International Journal of Hydrogen Energy 104 (2025) 584–598

Contents lists available at ScienceDirect

International Journal of Hydrogen Energy

journal homepage: www.elsevier.com/locate/he

# Solar-driven thermochemical water splitting: 3D energy flow analysis of a volumetric fixed-bed reactor design

Jörg Lampe [a,*], Sören Henke [a], Steffen Menz [a], Thomas Fend [b]

[a] RFH – University of Applied Science, Cologne, Engineering Faculty, Energy Technology, Vogelsanger Str. 295, 50825, Cologne, Germany
[b] German Aerospace Center (DLR), Institute of Future Fuels, Linder Höhe, 51147, Cologne, Germany

ARTICLE INFO

Handling Editor: Ibrahim Dincer

*Keywords:*
Solar fuels
Concentrated solar power
Water splitting
Hydrogen
Energy flow analysis
Physical modeling

ABSTRACT

A promising alternative to established methods for solar hydrogen generation is direct water splitting via thermochemical two-step redox cycling, which has the potential for highly attractive solar-to-fuel efficiencies. This paper presents results of a 250-kW prototype fixed-bed reactor, utilizing a hemispherical-shaped porous metal foam absorber. A complex multi-physical simulation model has been developed with fine local resolution of the size of thin slices of absorber blocks. The focus of this paper is on local energy flow analysis of hot spots, characteristic behavior of absorber temperature distribution in case of nonuniform irradiation and resulting influence on efficiency. Further, balancing effects of surface temperature inhomogeneities are analyzed by varying thermal conductivity of reactor materials, thereby reducing both surface and radial temperature differences: increasing the conductivity of the used tape material by a factor of 5 (or 20) the overall plant efficiency can be substantially improved by roughly 50% or 100%, respectively.

## 1. Introduction

Green hydrogen is gaining momentum in the ongoing development of future sustainable energy systems. It will play a crucial role in e.g. fuel cells [1], transportation [2,3], steel and chemical industry [4,5]; with related topics of hydrogen storage technologies [6–10], grid integration [11,12], and energy management [13,14]. In this context, it is of inherent importance to identify and promote efficient production technologies. While the established variant of using photovoltaics and subsequent electrolysis is a viable option, it is subjected to high losses due to the conversion of solar to electrical energy. A promising alternative is direct water splitting via employing a thermochemical two-step redox cycle. An overview of different aspects of this technology is given in Refs. [15–17]. The main advantage of this approach is the direct conversion of sunlight into fuel, which offers highly attractive potential solar-to-fuel efficiencies of up to 40%. This, in combination with fast chemical reaction kinetics of suitable reactive materials, makes the process technically and economically very interesting. Several different plant designs have been developed, as e.g., with a fixed bed reactor [18,19], particle reactor bed [20] as well as a rotating particle reactor [21] and with a fluidized reactor bed [22]. The focus in the last years has been set on ceria as viable redox material, see Refs. [23–25] and [26]. Research is ongoing regarding overall reactor and plant design [16,24], structure of the absorber [27,28], its reactive material [29–31] and [32], an efficient operational strategy [33–35], and general economic studies [36,37]. Up to now a plant efficiency of 5% has been successfully demonstrated for a lab-scale prototype in Ref. [18]. A promising step forward might be the usage of perovskites instead of established ceria, with a corresponding novel reactor concept proposed in Ref. [38].

This paper presents the results of a 250-kW prototype fixed-bed reactor with a hemispherical-shaped porous metal foam absorber made of ceria. In previous works the authors have presented a complex multi-physical simulation model, which considers detailed material and technical properties, at a comparable coarse level of spatial resolution. This model has been validated via data from several measurement campaigns, cf [39,40]. In related studies [41,42], the model has been used to analyze physical system behavior and energy flow of the complete pilot plant. Additionally, the model has been utilized in Refs. [33,34] to determine optimal operational process strategies.

In this work, the existing multi-physical reactor model has been substantially extended by enhancing the spatial resolution and adapting related energy transfer mechanisms both at the surface and inside the absorber. Thus, the 3D model can now depict not only rotationally symmetric behavior, but also local effects of the size of 1–2 mm slices of

* Corresponding author.
*E-mail address:* Joerg.Lampe@rfh-koeln.de (J. Lampe).

https://doi.org/10.1016/j.ijhydene.2024.08.386
Received 26 November 2023; Received in revised form 10 June 2024; Accepted 23 August 2024
Available online 4 September 2024

absorber metal foam blocks.

The main contribution of this work are detailed investigations on the effect of inhomogeneous solar irradiation on fixed-bed reactors and potential countermeasures. The focus is on local energy flow analysis of hot spots, characteristic behavior of absorber temperature distribution due to nonuniform irradiation and resulting influence on solar-to-fuel efficiency. Further, the balancing effect of surface temperature inhomogeneities is analyzed by variation of reactor material thermal conductivities. It is found out that by using a tailored tape material with a five times higher conductivity, and thereby using it as a heat bridge to deeper radial layers, the plant efficiency can be increased by 50%. Employing a tape with 20 times larger thermal conductivity, or alternatively 10 times larger conductivity of the absorber material itself, the plant efficiency even doubles. These findings should be taken into consideration for future reactor designs and heliostat field target point strategies.

The structure of the paper is as follows. Firstly, the reactor design is described, followed by the presentation of the refined thermochemical and optical simulation model, which includes results on mesh refinement. The model is then employed within several case studies on inhomogeneous solar irradiation, influence of material properties on absorber temperature behavior and resulting plant efficiency. Finally, conclusions and outlook are given.

## 2. Reactor and absorber design

The governing chemical reaction equations of the two redox steps are as follows:

$$CeO_{2-\delta_{ox}} \xrightarrow{+\Delta h_{red}} CeO_{2-\delta_{red}} + \frac{1}{2}(\delta_{red} - \delta_{ox})O_2, \quad (1)$$

$$CeO_{2-\delta_{red}} + (\delta_{red} - \delta_{ox})H_2O \xrightarrow{-\Delta h_{ox}} CeO_{2-\delta_{ox}} + (\delta_{red} - \delta_{ox})H_2. \quad (2)$$

The first equation indicates the reduction step, in which ceria is non-stoichiometrically reduced within an environment containing as little oxygen as possible. The non-stoichiometric coefficients before and after the reaction are denoted as $\delta_{ox}$ and $\delta_{red}$, with $\delta_{red} > \delta_{ox}$. The reduction step (1) is endothermic, thus is preferably conducted at high temperatures. In the subsequent oxidation step (2) the ceria is oxidized by injected steam to the same oxidation level as in the beginning of the reduction step, such that the cycle is closed. Hence, this second step is the actual water splitting, i.e., the hydrogen generation step. Since the oxidation step runs exothermically, a comparable lower temperature is beneficial.

The reactor and plant design of the prototype investigated in this paper has been developed within a couple of preceding projects by international partners, see Refs. [19,43,44] for more details on historic background. The main input parameters for the simulation model are given in Table 1.

**Table 1**
Simulation model input parameters.

| Description | Parameter | Value | Unit | Ref. |
|---|---|---|---|---|
| Ambient temperature | $T_{amb}$ | 298 | K | |
| Transmittance of quartz window | $\tau_{window}$ | 0.918 | | [59] |
| Absorbance of quartz window | $\alpha_{window}$ | 0.014 | | [59] |
| Reflectance of quartz window | $r_{window}$ | 0.068 | | [59] |
| Area of quartz window | $A_{window}$ | 0.32 | $m^2$ | |
| Absorber absorption coefficient | $a_{abs}$ | 0.6 | | |
| Absorber surface area | $A_{abs}$ | 1.707 | $m^2$ | |
| Absorber thickness | $t_{abs}$ | 60 | mm | |
| Absorber emissivity | $\epsilon_R$ | 0.6 | | |
| Absorber porosity | $\varepsilon$ | 0.65 | | |
| Absorber extinction coefficient | $\beta$ | 460 | $m^{-1}$ | [58] |
| Absorber mean pore diameter | $d_p$ | 2.27 | mm | |
| Absorber total ceria mass | $n_{ceria}$ | 377 | mol | |
| Absorber weight | $\omega_{abs}$ | 217 | kg | |
| $N_2$ specific production energy | $e_{N_2}$ | 15 | kJ/mol | [55] |
| Hydrogen higher heating value | $HHV_{H_2}$ | 39.41 | kWh/kg | |

A sketch of the reactor is displayed in Fig. 1, see Ref. [41] for a detailed description of design and material properties. Since the focus of this work is on the reactor, and particularly the inner absorber, the description of additional plant components such as heliostats field, heat exchangers, vaporizers, valves, and corresponding control is omitted here. We refer to Refs. [33,39–42] for detailed information and results on these aspects.

Reaction temperature is reached by concentrating solar radiation (CSR) via a heliostat field onto the quartz window, displayed on the left of Fig. 1. Most of the applied solar radiation enters the dome-shaped reactor chamber and heats up the absorber and fluids. In the first step (1) nitrogen with a purity of 0.99999 is inserted as flush gas at the inlet. Nitrogen follows the path indicated by the arrows in Fig. 1, enters the chamber through the outer ring and is guided by a slight overpressure through the absorber foam structure. Thereby, the nitrogen purges out oxygen via the outlet. In the second step (2) steam is provided at the inlet, which then follows the same path as the nitrogen before and is finally split via oxidation of the ceria. The generated hydrogen is led to the outlet in a wet steam atmosphere for subsequent drying treatment. Typical temperatures during reduction and oxidation step are 1400 and 1000 °C, respectively.

The heart of the reactor is the dome-shaped absorber with a maximal inner diameter of 600 mm corresponding to a total absorber irradiated surface area of 1.7 $m^2$. It consists of metal oxide foam block elements made from ceria and zirconia, with a thickness of 60 mm and an average porosity of $\varepsilon = 0.65$. The underlying foam structure is of zirconia, which is then coated by the reactive ceria, with volumetric fractions of 75 and 25%, respectively. Zirconia is used for mechanical stability; it does not take part at the chemical reaction. The absorber is attached to a holding structure within the inner vessel, which is embedded in the outer vessel with a suitable insulation. The overall thermal limit of the absorber surface is at 1400 °C, caused by technical limitations of the window flange, which itself is indirectly heated up by thermal radiation from the absorber surface.

In Fig. 2 a detailed drawing of the absorber is given, showing the arrangement of the absorber block elements. In the exploded view on the right six torus-shaped components denoted as S1 to S6 are displayed, consisting of 18 single absorber elements each. Each element is enumerated by a number from 1 to 18, as indicated in the front view on the left. The inner center disc is denoted as segment S7 and is constructed as one single absorber block. Note that the inner surface of the segments S1 and S2 are not visible in the front view due to the geometric shape of the absorber. In total the absorber is composed of 109 structural blocks. To properly capture local phenomena in the simulation model, a mesh refinement study has been carried out, with results presented in the next chapter. Different spatial discretizations are investigated, i.e., on element block level as well as in radial flow direction by slicing single

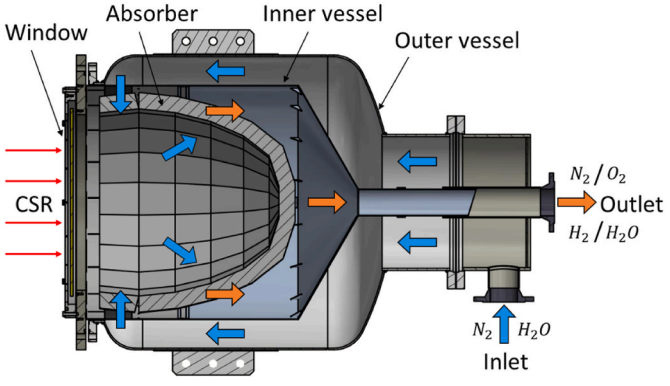


**Fig. 1.** Reactor design concept.

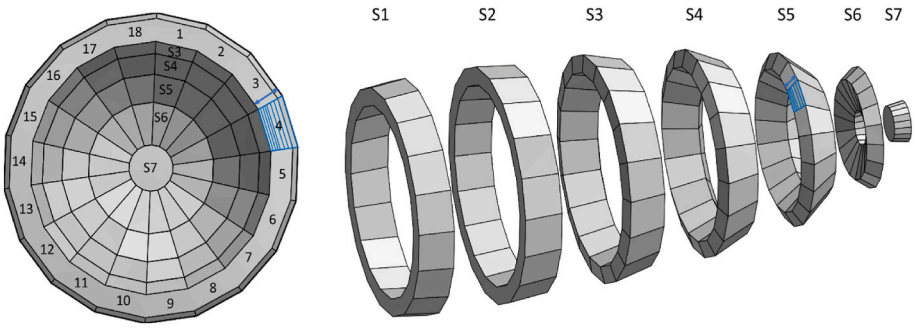


**Fig. 2.** Absorber 3D drawing – Left: Front view – Right: Lateral sliced view.

blocks, as indicated in Fig. 2 on the left at block number 4, and on the right within segment S5.

## 3. Thermochemical and optical simulation model

The typical operating process for the two-step redox cycling is the temperature swing scenario. The reduction step (1) is conducted at highest feasible surface temperature, which here is $\vartheta_{red} = 1400$ °C. Depending on the design of the plant, range and duration of efficient temperature swing strategies vary. For efficient operation the oxidation step (2) is conducted at lower temperatures at around $\vartheta_{ox} \approx 1000$ °C, corresponding to a $\Delta\vartheta \approx 400$ °C. Large temperature swings correspond to a temperature difference of $\Delta\vartheta \approx 600$ °C, and small temperature swings to $\Delta\vartheta \approx 200$ °C. Isothermal operation has drawbacks due to a decreased oxidation level and a significantly increased amount of required steam in step (2), cf [34,45,46]. Nevertheless, for very high feasible temperatures this might be an option due to fast cycling and the absence of thermal management. Please refer to Refs. [20,33,34,47–49] for more details on most efficient operation, and to Refs. [20,24,25,31,41,49–54] for experimental and simulation results for different operational modes and various conditions for running the process.

In this paper the usage of the term efficiency is defined as the plant efficiency by the following expression:

$$\eta_{plant} = \frac{m_{H_2} \bullet HHV_{H_2}}{Q_{sol} + E_{el,vap} + m_{N_2} \bullet e_{N_2}}, \tag{3}$$

with the amount of generated hydrogen $m_{H_2}$ in kg, hydrogen higher heating value $HHV_{H_2}$ in J/kg, applied solar and vaporization energy for steam generation $Q_{sol}$ and $E_{el,vap}$ in J as well as the total mass of needed nitrogen for the reduction $m_{N_2}$ in kg, and the related specific production energy $e_{N_2}$ in J/kg, cf [55]. All values are with respect to one complete cycle.

In the remainder of this section the used enhanced simulation model is presented. A basic version of the model had already been introduced in preceding works [33,40,41], where the model has been validated by measurement data. The focus here is on accurately capturing local process behavior, and the related extension of the model regarding high spatial resolution. This leads to a much more complex model, especially by including all occurring optical effects. After a brief description of applicable thermodynamic equations, the optical model is presented, followed by a mesh refinement study for the spatial discretization.

### 3.1. Description of thermochemical model

Here a short introduction into some of the applicable thermodynamic effects and corresponding model equations is given. A detailed description can be found in Refs. [33,41].

The simulation model is built up as a physical model using the Simscape toolbox from Matlab, cf [56]. Several standard components have been extended for an increased temperature range, e.g., for capturing the characteristic behavior of employed fluid and solid material. The governing chemical reaction rate for the process is defined via:

$$\frac{d\delta}{dt} = \left[ (\delta_{max} - \delta) \bullet A_{red} \bullet e^{\frac{-E_{a,red}}{R \bullet T}} - \delta \bullet {p_{O_2}}^n \bullet A_{ox} \bullet e^{\frac{-E_{a,ox}}{R \bullet T}} \right] \bullet \gamma, \tag{4}$$

with $\delta$ as the average reduction extent of the ceria in equations (1) and (2), the theoretically maximal change in non-stoichiometry $\delta_{max}$, frequency factors $A_{red}$ and $A_{ox}$ for reduction and oxidation in $s^{-1}$ and $s^{-1} \bullet bar^{-n}$, corresponding activation energies $E_{a,red}$ and $E_{a,ox}$ in J/mol, universal gas constant $R$ in J/(mol • K), partial pressure of oxygen $p_{O_2}$ in bar, and the empirical factor $n$, cf [46]. The chemical reaction kinetic in squared brackets has been extended by considering applicable conversion rates within the factor $\gamma$, considering the actual and required amount of steam and nitrogen for thermodynamically conducting oxidation and reduction, cf [45]. The underlying static equilibrium relations have been worked out in Ref. [55], i.e., by regarding thermodynamic limits and criteria for Gibbs's energy. For the reduction step the value $\gamma$ is set to one, because more nitrogen than required for the static equilibrium is supplied in our prototype set-up. During oxidation, the equilibrium conversion ratio of steam to hydrogen is typically quite high which might require a larger amount of steam compared to the actual available amount of steam in a local volume element. For the oxidation, the value of $\gamma$ is defined as

$$\gamma(T, T_{red}, P_{O_2}, \alpha) = min\left( \frac{n_{H_2O,act}}{n_{H_2O,req}(T, T_{red}, p_{O_2}, \alpha)}; 1 \right), \tag{5}$$

with $n_{H_2O,act}$ as the amount of actual available steam for water splitting in mol, and $n_{H_2O,req}$ as the amount of required oxidiser in mol for generating one mol $H_2$ per mol ceria, depending on the actual temperature $T$, preceding reduction temperature $T_{red}$, oxygen partial pressure and the fraction completed for oxidation reaction $\alpha$. For $n_{H_2O,act}/n_{H_2O,rec} < 1$ the generation of hydrogen is reduced by the factor $\gamma$. For steam ratios $n_{H_2O,act}/n_{H_2O,rec} > 1$ the factor $\gamma$ is limited by one, i.e., the reaction rate only depends on the kinetic formulation.

For a spatial element of the reactor conduction, convection, extinction, and radiation mechanisms may apply, depending on its location. Additionally, for elements of the absorber mass and heat transfer through porous media must be considered, cf [57,58]. Conservation of energy for the solid absorber material is regarded by:

$$(1 - \varepsilon) \bullet \rho_s \bullet c_{p,s}(T_s) \bullet \frac{\partial T_s}{\partial t} = \nabla((k_s + k_r) \bullet \nabla T_s) + \dot{Q}_{fs}, \tag{6}$$

where the material density in $kg/m^3$ is denoted by $\rho_s$, the corresponding porosity by $\varepsilon$, the specific heat capacity in J/(kg • K) by $c_{p,s}$, solid temperature in $K$ by $T_s$, effective and radiative conductivity in W/(m • K) by $k_s$ and $k_r$, and heat transfer at the interface of solid and fluid in $W/m^3$ by $\dot{Q}_{fs}$. Further, conservation of fluid energy is regarded via:

$$\varepsilon \bullet \rho_f \bullet c_{p,f} \bullet \frac{\partial T_f}{\partial t} + \nabla\left(\varepsilon \bullet \rho_f \bullet c_{p,f} \bullet u \bullet T_f\right) = \nabla\left(k_f \bullet \nabla T_f\right) + \dot{Q}_{fs}, \tag{7}$$

where the fluid density in kg/m$^3$ is denoted by $\rho_f$, fluid specific heat capacity in J/(kg • K) by $c_{p,f}$, fluid velocity in m/s by $u$, temperature of fluid in K by $T_f$, and its thermal conductivity in W/(K • m) by $k_f$.

The attenuation and absorption of incoming solar energy flow applies to elements located at the first radial surface layers, which is regarded by the Lambert-Beer law:

$$\dot{Q}_{sol,abs}(z) = \dot{Q}_{sol,abs}(0) \bullet e^{-\beta \bullet z}, \tag{8}$$

where the amount of the solar energy flow $\dot{Q}_{solar,abs}$ reaching a material depth $z$ in m, depends on the available energy flow at the surface in W/m$^2$ and the coefficient of extinction $\beta$ in 1/m. Note that heat radiation applies to the same spatial elements.

The following further general assumptions for the simulation model have been made:

- Structure of porous material of the absorber is homogeneous
- All ceria in the absorber takes part at chemical reaction
- Absorber behaves optically as gray body
- All occurring gases are transparent
- Provided solar power is distributed homogeneously onto considered surface elements
- Power adjustment from heliostat field is continuous
- Adjustment of heliostat field power is realized by a fast controller using the surface temperature of the absorber

### 3.2. Description of optical model

The focus of this paper is on accurately capturing local effects, which is related to a fine discretization of the absorber. Besides the radial discretization, in particular a high spatial resolution of the absorber surface area is highly desirable, cf. Fig. 2. Increasing the level of radial discretization goes along with a linear increase of thermodynamic conversion equations for all discrete volume elements, whereas the complexity of the optical model increases roughly quadratic with the number of surface elements. In this section, some background on applicable optical effects and their implementation are presented.

The incoming solar flux from the heliostat field $\dot{Q}_{sol}$ for heating up the absorber first reaches the quartz window at the aperture of the reactor, see Fig. 3. The optical properties of the used window are frequency dependent, see Ref. [59], and the effective coefficients for reflectance, transmission and absorption have been determined by integration over the solar spectrum, cf [60]. The resulting optical efficiency in terms of provided irradiation into the reactor is 93%, including 1% of absorption, see Ref. [40] for more details.

Reflected and absorbed solar radiation $\dot{Q}_{sol,r}$ and $\dot{Q}_{sol,a}$ are not reaching the inner reactor, however, the largest part $\dot{Q}_{sol,\tau}$ is transmitted through the window and hits the absorber surface. A large part of this energy flow directly heats up the absorber surface, which is denoted by $\dot{Q}_{S1,a}$ for the upper absorber element in segment S1, and a smaller part is reflected onto other surface elements or the quartz window, here denoted by $\dot{Q}_{S1,r}$.

This leads to an optical network for the solar radiation considering reflections and re-reflections, partly back to the environment through the window. Additionally, heating up the absorber to temperatures above 1000 °C leads to a further significant radiation source: heat radiation from absorber surface layers, where the same optical mechanisms apply. In Fig. 3 general heat radiation is given as $\dot{Q}_{S1,heat}$ and $\dot{Q}_{S7,heat}$, reflections as $\dot{Q}_{S2,r}$, re-reflections as $\dot{Q}_{heat,r}$, absorption as $\dot{Q}_{S2,a}$ and $\dot{Q}_{heat,a}$, and transmission is denoted as $\dot{Q}_{heat,\tau}$.

In the simulation model the two radiation sources are captured by the same optical network. Here it is employed the radiosity method which assumes reflections as diffuse radiation, cf [61]. This assumption

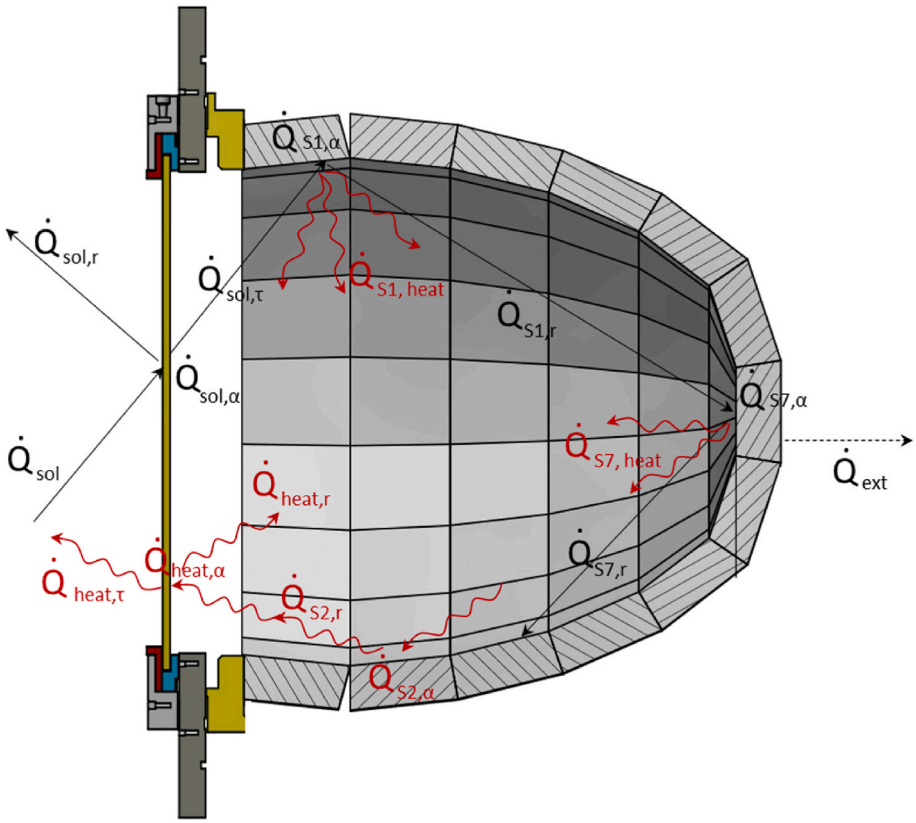


**Fig. 3.** Sketch of solar and heat radiation effects.

is considered as suitable due to the open foam structure of the porous absorber.

The radiosity $H_i$ in W/m$^2$ of a discrete surface element i is given by

$$H_i = \sigma\varepsilon T_i^4 + (1-\varepsilon)\cdot E_i, \tag{9}$$

with the Stefan Boltzmann constant $\sigma$ in W/$\left(\mathrm{m}^2\cdot\mathrm{K}^4\right)$, $\varepsilon$ as emissivity, $T_i$ as temperature in K, and $E_i$ as the irradiance in W/m$^2$ onto this element. The following relation for the irradiance is based on the radiosity of all n surface elements involved, together with their corresponding areas $A_i$ in m$^2$ and view factors $F_{j\to i}$ from surface element j to i:

$$E_i = \sum_{j=1}^{n} \frac{F_{j\to i}\cdot A_j}{A_i}\cdot H_j = \sum_{j=1}^{n} F_{i\to j}\cdot H_j. \tag{10}$$

The second equality holds by the reciprocity relation $F_{j\to i}\cdot A_j = F_{i\to j}\cdot A_i$. With (9) and (10) it holds

$$H_i = \sigma\varepsilon T_i^4 + (1-\varepsilon)\cdot\sum_{j=1}^{n} F_{i\to j}\cdot H_j, \text{for} \quad i=1,\ldots,n, \tag{11}$$

for all surface elements, yielding a linear system of equations for the radiosities. Given these radiosities the resulting heat flows can be determined via the energy flow balance

$$\dot{Q}_i = A_i(H_i - E_i) = \frac{A_i\varepsilon_i}{1-\varepsilon_i}\left(\sigma T_i^4 - H_i\right), \text{for} \quad i=1,\ldots,n. \tag{12}$$

The view factors $F_{i\to j}$ occurring in equation (10) are of particular importance in this work since they heavily influence the heat distribution on the absorber surface. In the simulation model they are reflected by a thermal conductance network with the reciprocal view factors as corresponding thermal resistors. The values of the view factors have been determined with a 3D-CAD model of the absorber using ANSYS [62].

### 3.3. Mesh refinement study

For properly capturing local effects a suitable spatial discretization must be chosen. The dominant spatial dependent behavior of the reactor is the temperature gradient from the absorber surface to backside, denoted as its radial direction. Since this effect strongly influences hydrogen generation, it is important to ensure the grid independence. Therefore, a radial mesh refinement study has been carried out, where the thickness of radial slices has been chosen up to 1 mm, which is about half the average pore diameter of the metal foam. To further account for effects occurring due to non-uniform solar irradiation the absorber is also meshed with respect to its surface, i.e., orthogonal to the radial direction. Thus, this discretization is denoted as orthogonal mesh, which has not been investigated by the same granularity as the radial direction due to the quadratically increasing complexity of the optical part of model. The finest implemented orthogonal mesh is at the level of element blocks with an average surface area of 11 × 14 cm, cf. Fig. 2, but without including the roughly 12 thousand corresponding view factors due to computational software and hardware capacities. Thus, the finest orthogonal mesh considered here is on the level of double blocks, where all optical solar and heat radiation effects are regarded by good three thousand view factors. In the remainder of this section, results on the radial and orthogonal mesh refinement are presented.

#### 3.3.1. Radial mesh refinement

For the radial discretization, the 60 mm blocks are divided into a front section with depths from 0 to 16 mm, a mid-section for depths between 16 and 54 mm, and a fixed back section of 6 mm thickness. Front and mid-section are subjected to mesh refinement, whereas the back section is kept fixed as one layer. The back layer contains the thermocouple sensors used in Refs. [39,40] and accounts for radiation and extinction effects between absorber backside and inner vessel, cf. Fig. 1. The size of the front section has been chosen regarding the penetration depth of solar radiation. In the mid-section thermodynamic effects of conduction, convection, thermochemical reaction, fluid flow, and heat radiation through porous media are accounted for. The coarsest mesh denoted as “1 + 1” consists of one front element of 16 mm thickness, one middle element of 38 mm thickness, and the fixed back element of 6 mm. All investigated meshes consider an identical number of layers in front and mid-section. The finest radial mesh “16 + 16” consist of 16 slices in the front area of 1 mm each, 16 slices in the middle section of 2.375 mm each, and the fixed back layer. For all radial meshes the orthogonal discretization of the absorber has been chosen as the seven ring segments displayed in Fig. 2, which implies a constant temperature of a thin layer throughout a ring segment.

For the mesh refinement study a typical base case scenario is considered, see e.g. Ref. [41]. This consists here of a 60-min heat-up phase using three power steps and then three subsequent cycles of 20 min reduction with 100 kg/h nitrogen and 20 min oxidation with a steam flow of 15 kg/h.

In Fig. 4 the homogeneously applied solar power is shown together with the temperature of absorber surface and backside, averaged over all absorber segments, for the 4 + 4 mesh over 3 h. The maximum solar power of 271 kW is used in the beginning of the reduction step and drops to 228 kW at the end of reduction. Within an oxidation step the solar power ranges between 0 and 28 kW. The surface temperature nicely follows the set-point temperatures of 1400 °C during reduction and 800 °C during oxidation. The temperature at the back of the absorber behaves much slower, related to a much smaller temperature range between 1120 and 850 °C.

The temperature behavior of all radial layers for the finest 16 + 16 mesh can be found in Figure 12 in the appendix. The front and back layer temperature curves of the 16 + 16 mesh are very similar to the ones from the 4 + 4 mesh in Fig. 4.

To investigate the dependency of radial mesh size and corresponding temperature behavior, front, back and inner back temperatures at the times $t_1$ and $t_2$ are compared. The time $t_1$ is at the end of reduction at 9500 s and $t_2$ is at the end of oxidation at 10800 s, see also Fig. 4. The meaning of front and back temperatures are the temperatures of the surface and fixed back layer, and the meaning of inner back is the second last layer, directly before the backside. Note, that the thickness of front and inner back layer varies over the mesh sizes.

In Fig. 5 the convergence history for the three temperatures at the times $t_1$ and $t_2$ is displayed for increasing mesh sizes. What can be seen on the left is a converging behavior for the surface and backside temperature at the end of reduction at $t_1$. The surface temperature increases from around 1399 °C by 9 °C–1408 °C when increasing the mesh size from 1 + 1 to 16 + 16. Also, the backside temperature just ranges from 1128 °C for the 1 + 1 mesh to 1120 °C for the finest mesh. Only the temperature of the inner back layer significantly differs by starting from

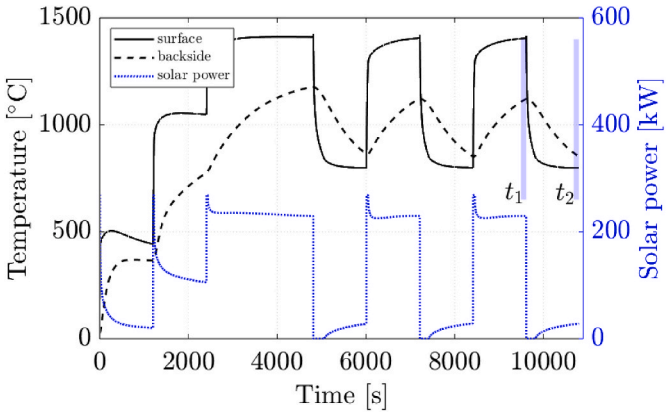


**Fig. 4.** Behavior of absorber front and back temperature during process operation using a 4 + 4 mesh.

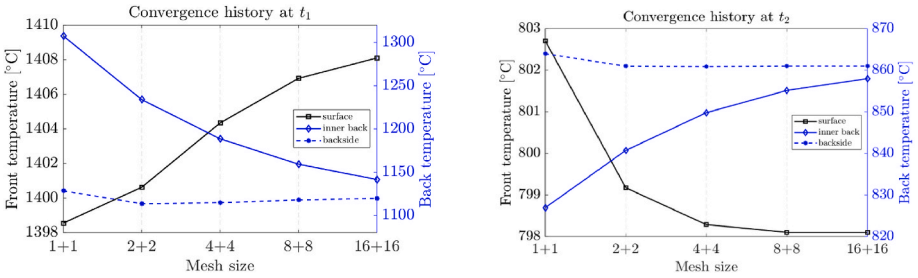


**Fig. 5.** Convergence history for average front and back temperatures over the mesh size.

1307 °C for the coarsest mesh to 1142 °C for the finest mesh. This is the expected behavior, since the second last layer gets thinner over the radial mesh refinement, hence the corresponding discrete element is smaller in volume and thereby also smaller in heat capacity, thus its temperature approaches the one of the fixed back layer. A similar behavior can be obtained from the plot on the right of Fig. 5 for the end of oxidation at time $t_2$. The surface and backside temperatures are again converging to a final value of 798 and 861 °C respectively. The only difference is the direction of monotonic convergence of surface and inner back temperature, which is due to the reverse process of heating up and cooling down during reduction and oxidation. Again, the inner back temperature is nicely approaching the back layer temperature.

Along with the radial temperature distribution the amount of generated hydrogen also depends on the mesh size. The corresponding values of one cycle are given in the following Table 2.

The obtained amount of 5.81 g $H_2$ per cycle for the finest mesh is used here as the actual generated amount, and thus the relative difference is given with respect to this value. The generated hydrogen does not vary much for finer meshes, i.e., less than 3% for the 4 + 4 mesh and less than 1% for the 8 + 8 mesh. The slow decrease in generated hydrogen over the mesh size can be explained by the finer resolution of the front layers. The temperature of the surface layer does not vary that much, as it can be seen in Fig. 5, and the coarser meshes cannot capture exactly the smooth radial temperature gradient of the finer meshes, cf. Figure 12, and thereby a coarse mesh overestimates the temperatures of the layers behind the surface layer of a finer mesh. This hotter radial front region is related to a larger amount of hydrogen generation for the rougher meshes, cf. Table 2.

The corresponding computation time and solver statistics are summarized in Table 3 for all investigated mesh sizes.

All simulations have been carried out on a desktop PC with an Intel core i9-12900K CPU with 16 physical kernels running at 3.2 GHz with 32 GB RAM, using the software version Matlab R2021a. In the second row of Table 3 the number of variables of the corresponding system of differential algebraic equations is displayed, here denoted as no. of states. The number of states increases from around 2000 to more than 11000 for the finest mesh. The total number states within a model consist of roughly 1150 states for capturing the behavior of the outer parts of the reactor as e.g., insulation, piping, valves, heat exchangers, whereas the remaining variables represent the absorber. The number of absorber related states is proportional to the number of discrete elements of a mesh, i.e., around 900 for the 1 + 1 mesh (3 layers), to 1500 for the 2 + 2 mesh (5 layers), up to 10000 for the 16 + 16 mesh (33 layers).

The computation time in the third row increases roughly linear with the number of variables up to the 8 + 8 mesh, and then enters a cubic relation in the final mesh refinement step. Thus, it can be assumed that this also holds for a further mesh refinement, i.e., doubling the variables results in a factor 8 for the computational time. The related run/sim-time ratios in the fourth row can be directly calculated from the computational time and the fixed 3 h simulation time, cf. Fig. 4. The number of solver steps slightly increases for the first mesh sizes and then roughly doubles for the finest mesh. The average solver step sizes in the last row are obtained accordingly from the required number of steps. Thus, for this set-up the radial 8 + 8 mesh is regarded as a suitable compromise between accuracy and performance, i.e., for the considered basic orthogonal discretization of 7 segments.

**Table 2**
Generated hydrogen within one cycle for different mesh sizes.

| Mesh size | 1 + 1 | 2 + 2 | 4 + 4 | 8 + 8 | 16 + 16 |
|---|---|---|---|---|---|
| $H_2$ per cycle [g] | 8.47 | 6.50 | 5.98 | 5.85 | 5.81 |
| Rel. difference [%] | 44.48 | 11.54 | 2.84 | 0.67 | 0 |

**Table 3**
Model and solver statistic for different radial mesh sizes.

| Mesh size | 1 + 1 | 2 + 2 | 4 + 4 | 8 + 8 | 16 + 16 |
|---|---|---|---|---|---|
| No. of states | 2056 | 2662 | 3874 | 6306 | 11154 |
| Computation time [s] | 349.4 | 625.2 | 873.1 | 1229.2 | 7158.4 |
| Run/Sim-time ratio | 0.03 | 0.06 | 0.08 | 0.11 | 0.66 |
| No. of solver steps | 13923 | 14152 | 14512 | 15220 | 30511 |
| Average step size [s] | 0.78 | 0.76 | 0.74 | 0.71 | 0.35 |

### 3.3.2. *Orthogonal mesh refinement*

For the radial refinement the segmentation of the absorber into the annular ring segments S1 to S6 and the center disc S7 has already been considered, cf. above paragraph and Fig. 2. For the orthogonal mesh refinement these segments are now further divided into 3 and 9 elements respectively. Cutting an annular segment into three parts corresponds to combined orthogonal elements $S_{Si,1-6}, S_{Si,7-12}, S_{Si,13-18}$ for $i = 1, \ldots, 6$ having the same temperature and energy state in a specific radial layer. Thus, one combined element of the S1 to S6 ring consists of six single block elements, cf. Fig. 2. For the investigation of the orthogonal mesh, a fixed radial 4 + 4 mesh is applied in all cases, i.e., considering nine radial layers. The first orthogonal discretization is denoted as O3, and the related absorber model consists of $7 \cdot 3 \cdot 9 = 189$ elements. Note, that in the model the center disc has also been subdivided into three parts, whereby all parts of the disc are assumed to have the same temperature. Accordingly, using 9 elements per annular segment is denoted as O9, which is related to an absorber model consisting of $7 \cdot 9 \cdot 9 = 567$ elements, where again the center disc has been subdivided as well. The orthogonal elements of the O9 mesh are double block elements given by $S_{Si,1+2}, S_{Si,3+4}, \ldots, S_{Si,17+18}$ for $i = 1, \ldots, 6$. The corresponding size of a double block surface area roughly is 22 × 14 cm, slightly varying with the location in the absorber. The number of the total absorber elements of the O9 mesh is much larger compared to the finest radial 16 + 16 mesh due to the larger number of absorber elements of 567 vs. $7 \cdot 33 = 231$. The related modeling effort has been significantly higher, especially due to implementing over 3000 view factors for the optical part of the O9 model. In contrast, the number of view factors considered in the radial mesh refinement has been 64, only considering one surface area for quartz window and each of the ring segments S1 to S7. In the following this basic mesh is denoted as O1.

For demonstrating the influence of different mesh sizes, a scenario

with only five irradiated double block elements is regarded. The five elements form a cross, with element $S_{S4,7+8}$ located in the middle. The applied solar power for each of the four outer elements is the area weighted profile shown in Fig. 4, ie., at the end of reduction this is about 4.55 kW. The middle elements $S_{S4,7+8}$ constantly receives twice the amount of solar power. Thus, the same 3 h scenario as for the radial mesh refinement has been considered. On the right side of Fig. 6 the resulting surface temperature at the end of the reduction step for the O9 mesh is shown, and on the left side for the O3 mesh. The irradiated cross on the right cannot be captured correctly by the O3 mesh, since blurring occurs due to averaging over three neighboring elements from the O9. The elements $S_{S4,1+2}, S_{S4,3+4}, S_{S4,5+6}$ of the O9 are summarized to the combined element $S_{S4,1-6}$ in the O3, and the same holds for $S_{S4,7+8}, S_{S4,9+10}, S_{S4,11+12}$ which are aggregated to $S_{S4,7-12}$, thereby deforming the cross. Note that the surface temperatures of the combined block elements are not simply averaged temperatures of the corresponding O9 elements since heat losses at the surface due to radiation are not linear in temperature. Thus, the higher resolution of the hot cross goes along with larger heat radiation losses to the environment. Thereby, the area-weighted average temperature of the absorber surface of the O9 mesh is roughly 30 °C lower compared to the O3 mesh. The reason for the colder temperature in segment S1 can be explained by the cooling effect of the fluid that enters the reactor through this absorber segment. For the corresponding temperature distribution at the absorber backside, please refer to Figure 13 in the appendix. Here, a similar qualitative temperature distribution can be observed, but since the heat energy has travelled radially through the absorber the cross-shape of the irradiated surface has been subjected to an additional kind of blurring. In Figure 14 and 15 the temperature distributions for O3 and O9 mesh at the end of the oxidation step are displayed for absorber surface and backside, where the above-described findings hold as well. The related results with the O1 mesh yield an even more blurred version of the temperature distribution with only one averaged temperature per segment.

The corresponding behavior of the computation time and solver statistics are displayed in Table 4 for the three investigated orthogonal mesh sizes.

**Table 4**
Model and solver statistic for different orthogonal mesh sizes.

| Mesh size | O1 | O3 | O9 |
|---|---|---|---|
| No. of states | 3874 | 9667 | 27765 |
| Computation time [s] | 882.2 | 2485.1 | 17835.6 |
| Run/Sim-time ratio | 0.08 | 0.23 | 1.65 |
| No. of solver steps | 13710 | 13046 | 13033 |
| Average step size [s] | 0.76 | 0.83 | 0.83 |

Note, that the O1 mesh is identical to the radial 4 + 4 mesh, i.e., the corresponding number of states is the same and the corresponding performance values in column two of Table 4 are similar to those of column four in Table 3. Here, the number of absorber related states triples from O1 to O3 and to O9 mesh, i.e., they increase from roughly 2700 in the O1 to about 25000 in the O9, and over 50000 in the O18 mesh. The total number of states of the O18 mesh is equal to 52031. Please note that no simulation results with the O18 are shown, since the view factors are not implemented. The computation time in the third row increases roughly linear with the number of variables from the O1 to the O3 mesh, and then enters a quadratic relation to the O9 refinement with a computation time of nearly 5 h. The related run/sim-time ratios are again obtained from the computation time and the 3 h simulation time. The number of solver steps roughly remains constant, and thereby also the average step size. When combining finer radial meshes with fine orthogonal meshes, the computational times get enormous and unpracticable due to their at least quadratic relation to the number of states, e.g., for a radial 16 + 16 mesh combined with the orthogonal O9 mesh the number of states is above 100,000. Overall, for the simulation of local effects of the absorber the orthogonal O9 mesh with the radial 4 + 4 mesh is considered as a suitable overall level of discretization.

## 4. Case study: Inhomogeneous solar irradiation and influence of material properties

Inhomogeneous irradiation can occur due to various reasons: geometry and positioning of the reactor on the solar tower in combination with the heliostat field may not allow the reflected solar radiation to uniformly cover the complete absorber surface, local shadowing of some of the heliostats in the field caused by scattered clouds, several dusty or dirty heliostats caused by environmental conditions and animals, or single erroneously positioned heliostats. This may either lead to larger inhomogeneous temperature regions at the absorber surface or to the occurrence of single hot spots. Since the resulting effects for the overall process are different, they are treated separately in the following case studies. Thus, in this section it is first carried out a hot spot energy flow study considering different surface and hot spot temperatures and related healing times, second the effect of inhomogeneous irradiation is investigated in case larger parts of the absorber surface area are completely or partly shadowed is investigated with regard to the plant efficiency, and third the beneficial influence of increased thermal conductivities of absorber and tape material is determined for the same considered cases of partly shadowing.

### 4.1. Hot spot energy flow analysis

In Fig. 7 a picture of the temperature distribution of the absorber surface of the investigated prototype is shown. The picture has been taken during a measurement campaign by an infrared thermal camera in the DLR Synlight solar lab in Julich, Germany, see Ref. [63] for some background on the facility. Two hot spots are visible with temperatures of around 1300 °C while the remaining surface is at around 1200 °C and below. Such hot spots can occur quite fast due to not properly adjusted heliostats, or in this case due to not properly adjusted high energy lamps

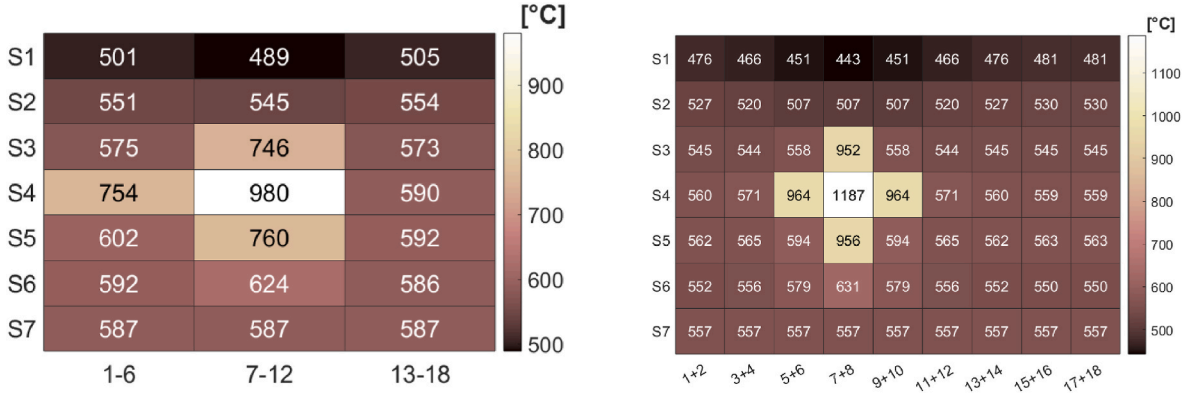


**Fig. 6.** Temperature of absorber surface at end of reduction – O3 mesh (left), O9 mesh (right).

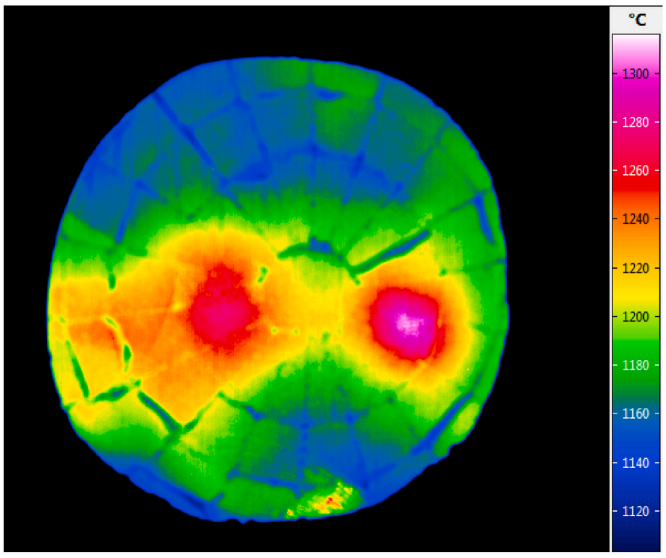


**Fig. 7.** Absorber surface temperature with two hot spots, photo by IR camera.

in the solar lab. Important questions related with this phenomenon are how much additional power is required to create hot spots of certain temperature gaps, how long does it take until the hot spot vanishes after it has been detected, and what are the main energy flows during the hot spot healing process. In Fig. 8 on the left the absorber surface temperature is displayed for a simulated hot spot with an average temperature gap of nearly $\Delta T = 400$ °C using the O9 mesh. The size of the hot spot is the surface area of the element $S_{4,7+8}$, which is comparable to the size of each of the two hot spots in Fig. 7. In the simulated scenario the absorber is first heated up by a uniform irradiation power of 82.5 kW, corresponding to a power density of 48.5 kW/m$^2$, which heats up the absorber to an average surface temperature of 1014 °C. The segment S1 is again colder due to its function as fluid inlet area. Here a constant nitrogen flow of 100 kg/h has been applied without conducting any redox cycling. The hot spot is then generated by applying an additional power of 6.6 kW on the element $S_{4,7+8}$ only. On the left side of Fig. 8 the hot spot steady state condition is shown, i.e., also the remaining elements have indirectly been heated up, with an average temperature that is around 25 °C larger than before. Detection of the hot spot is then simulated by removing the additional power onto the hot spot element and switch back to the uniform irradiation. In Fig. 8 on the right the surface temperature distribution is shown after 90% of the hot spot temperature gap has been vanished, which is denoted here as the 90%-healing time.

The hot spot healing time $t_{heal,x\%}$ is defined as the time that is required for the hot spot temperature $T_{HS}(t)$ to cool down by x% of the corresponding hot spot temperature gap $\Delta T = T_{HS}^{max} - T_{hom}$. Thus, it holds

$$T_{HS}\left(t_{heal,x\%}\right) = T_{hom} + \left(1 - \frac{x}{100}\right)\cdot\left(T_{HS}^{max} - T_{hom}\right), \tag{13}$$

with $T_{HS}^{max}$ as the maximum hot spot temperature and $T_{hom}$ as the average level-off temperature in case of homogeneous irradiation.

The 90%-healing time in this example is roughly $t_{heal,90\%} = 60$ s, i.e., this is the time after which the remaining temperature gap is only 10% of the original gap $\Delta T$. Thus, here $\Delta T_{90\%} = (1-0.9)\cdot(1400°C - 1014°C) = 38.6°C$, with a corresponding hot spot temperature at the healing time of $T_{HS}\left(t_{heal,90\%}\right) = 1014°C + 38.6°C = 1053°C$, cf. Fig. 8 on the right. Running the simulation much longer will result again in the almost uniformly temperature distribution with an average of 1014 °C.

In Fig. 9 the different mechanisms occurring during the healing of the hot spot at element $S_{4,7+8}$ are displayed by corresponding arrows. The main release of energy takes place in the surface layer of the hot spot due to heat radiation to other absorber elements, the quartz window and partly back to the environment. The investigated outgoing energy flows for the surface layer of the hot spot element is the conductive heat

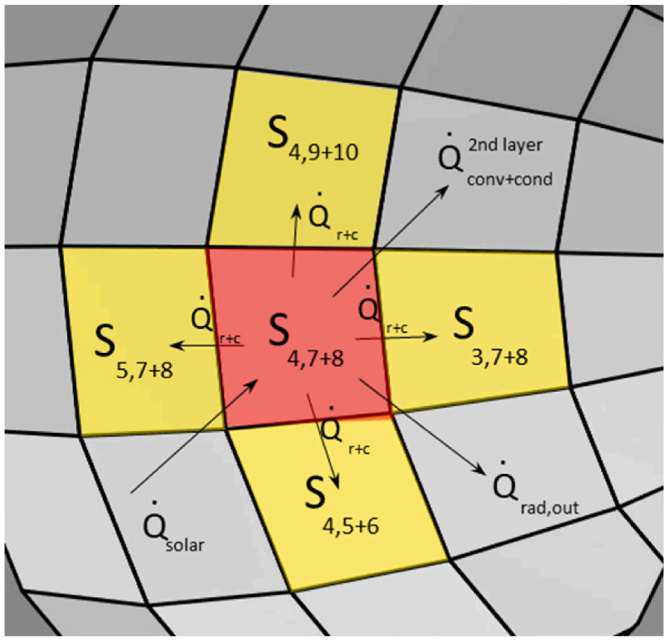


**Fig. 9.** Considered energy flows of the absorber hot spot surface layer.

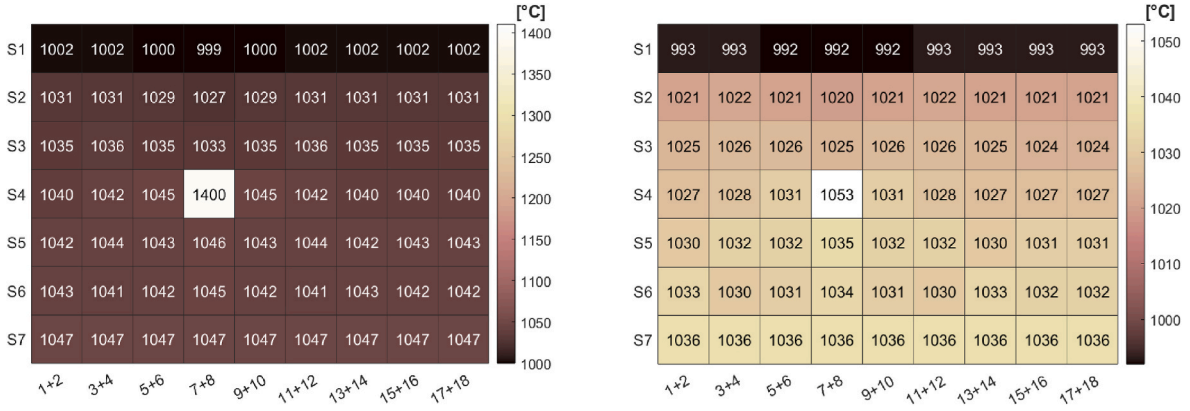


**Fig. 8.** Surface temperature with $\Delta T = 400$ °C hot spot (left), after 90%-healing time of 60 s (right).

transfer to the four neighboring elements ($\dot{Q}^{cond}_{S4,7+8\rightarrow S4,5+6}$, $\dot{Q}^{cond}_{S4,7+8\rightarrow S4,9+10}$, $\dot{Q}^{cond}_{S4,7+8\rightarrow S3,7+8}$, $\dot{Q}^{cond}_{S4,7+8\rightarrow S5,7+8}$) and to the next radial layer ($\dot{Q}^{cond,2nd\ layer}_{S4,7+8\rightarrow S4,7+8}$), convective heat transfer between porous material and fluid within the surface layer carried away by the fluid into the second radial layer ($\dot{Q}^{conv,2nd\ layer}_{S4,7+8\rightarrow S4,7+8}$), and the radiative heat transfer is split into the radiation onto to the four neighboring elements ($\dot{Q}^{rad}_{S4,7+8\rightarrow S4,5+6}$, $\dot{Q}^{rad}_{S4,7+8\rightarrow S4,9+10}$, $\dot{Q}^{rad}_{S4,7+8\rightarrow S3,7+8}$, $\dot{Q}^{rad}_{S4,7+8\rightarrow S5,7+8}$) and onto the remaining absorber surface elements and window ($\dot{Q}^{rad,out}_{S4,7+8\rightarrow rest}$). In Fig. 9 the arrows denoted with $\dot{Q}_{r+c}$ indicate the direction of radiative and conductive heat transfer to the neighboring elements. The ingoing energy flow is given by the solar power on the hot spot ($\dot{Q}^{solar}_{S4,7+8}$), and the difference between ingoing and outgoing energy flow is the change of inner energy of the hot spot element, i.e., proportional to the change of its temperature.

In Table 5 the energy flows introduced in Fig. 9 are evaluated for the hot spot in Fig. 8, ie., first after establishing the hot spot in a steady state condition, and second after the 90% healing time, which is here $t_{\mathrm{heal,90\%}} = 60\ s$.

In Table 5 the ingoing energy flows are displayed by a positive sign, whereas the outgoing flows are noted by a negative sign. The energy flows after building up the hot spot are given in the second column, where the zero in the last row indicates a steady state condition. The conductive heat transfer to neighboring elements is around 0.1 kW each, depending on the size of the corresponding interface area. The radiative heat transfer to the neighboring elements is between 0.05 and 0.2 kW, depending on the corresponding view factor. Here, the smaller angle between neighbor elements within one segment favors radiative heat exchange compared to those from other segments. The convection by the fluid into the second radial layer is comparable high with 0.6 kW, i.e., around four times larger than the conductive heat transfer to this second layer with 0.16 kW. The largest outgoing power is the combined radiative heat transfer to the surface layers of the remaining 50 elements of the O9 mesh and the quartz window. In the third column of Table 5 the energy flows for the situation shown in Fig. 8 on the right are given. The ingoing solar power is roughly 4 times smaller compared to the steady state hot spot. The energy flows due to conductive and radiative heat transfer are roughly half the values from the second column. The convection is significantly lower since the fluid is not substantially heated up in the surface layer any longer. Note, that the direction of the conductive heat transfer between the first two radial layers has changed, i.e., the cooling down of the first layer takes place much faster due to radiative heat losses, such that the second radial layer has a larger temperature after $t_{\mathrm{heal,90\%}} = 60\ s$, and thus slightly heats up the surface layer, cf. also Figure 12 in the appendix for a visualization of this effect. Summing up all ingoing and outgoing energy flows yields a difference of −0.34 kW, where the negative sign indicates a further cooling down of the hot spot element.

**Table 5**
Hot spot energy flows at steady state and after 90% healing time.

| Energy flow | power | [kW] |
|---|---|---|
| | at steady state hot spot | at 90% healing time |
| $\dot{Q}^{solar}_{S4,7+8}$ | +8.167 | +2.017 |
| $\dot{Q}^{cond}_{S4,7+8\rightarrow S4,5+6}$ | −0.074 | −0.039 |
| $\dot{Q}^{cond}_{S4,7+8\rightarrow S4,9+10}$ | −0.074 | −0.039 |
| $\dot{Q}^{cond}_{S4,7+8\rightarrow S3,7+8}$ | −0.112 | −0.060 |
| $\dot{Q}^{cond}_{S4,7+8\rightarrow S5,7+8}$ | −0.091 | −0.045 |
| $\dot{Q}^{rad}_{S4,7+8\rightarrow S4,5+6}$ | −0.202 | −0.106 |
| $\dot{Q}^{rad}_{S4,7+8\rightarrow S4,9+10}$ | −0.202 | −0.106 |
| $\dot{Q}^{rad}_{S4,7+8\rightarrow S3,7+8}$ | −0.086 | −0.045 |
| $\dot{Q}^{rad}_{S4,7+8\rightarrow S5,7+8}$ | −0.051 | −0.027 |
| $\dot{Q}^{conv,2nd\ layer}_{S4,7+8\rightarrow S4,7+8}$ | −0.606 | −0.045 |
| $\dot{Q}^{cond,2nd\ layer}_{S4,7+8\rightarrow S4,7+8}$ | −0.161 | +0.209 |
| $\dot{Q}^{rad,out}_{S4,7+8\rightarrow rest}$ | −6.511 | −2.051 |
| Sum | 0 | −0.335 |

In the following two tables results for investigated hot spots at element $S_{4,7+8}$ are presented for different temperature levels and temperature gaps regarding their 90%- and 95%-healing times, cf. equation (13). The simulated scenarios are analogue to the settings for the hot spot investigated above, with a nitrogen flow of 25 and 100 kg/h in Tables 6 and 7, respectively.

After steady state hot spot conditions are reached, the solar power is switched back to uniform radiation and the healing process starts. After reaching the healing temperatures $T_{HS}(t_{\mathrm{heal,90\%}})$ and $T_{HS}(t_{\mathrm{heal,95\%}})$ the corresponding times are recorded. The surface temperature in the first column is obtained when uniformly applying the stated solar power in column two. Additional power is required to generate a hot spot with the temperature gap ΔT between 100 and 600 °C as defined in column three. The applied power for generating a steady state hot spot is given in terms of a power factor in the fourth column. The power factor is defined as the ratio of total required solar power onto the element $S_{4,7+8}$ for generation of the hot spot and the uniform radiation onto this element during healing: $\dot{Q}^{solar,hotspot}_{S4,7+8}/\dot{Q}^{solar,hom}_{S4,7+8}$. The 90%-healing time in the fifth column mainly depends on the temperature level of the uniform radiation. The $t_{\mathrm{heal,90\%}}$ values are around 100 s for the temperature level 800 °C, 60 s for 1000 °C and 46 s for 1200 °C, thus, almost independent of the hot spot ΔT. Note that for a ΔT of 600 °C, i.e., with $T_{hom} = 800$ °C and $T^{max}_{HS} = 1400$ °C, the 90%-healing time means that the temperature of the hot spot has been cooled down from 1400 °C to 860 °C, whereas in the ΔT = 100 °C and $T_{hom} = 800$ °C case, the corresponding hot spot healing time considers the cooling down from 900 °C to 810 °C. Here, two effects for different ΔT values are in good balance in regard of the healing time duration, i.e., a larger absolute temperature difference of 0.9·ΔT that must be cooled down versus a larger hot spot starting temperature $T^{max}_{HS}$ with a significantly larger heat radiation favoring fast cooling down. When looking at the same ΔT for different temperature levels, a clear trend can be observed to faster cooling for larger homogeneous temperatures. This can be explained by the larger hot spot temperature $T^{max}_{HS}$ that is related to over-proportional heat radiation, cf. equation (9). The 95%-healing time in the last column is roughly two times the value of the 90% healing.

Increasing the fluid flow yields slightly faster cooling times displayed in Table 7, ie., the values of $t_{\mathrm{heal,90\%}}$ and $t_{\mathrm{heal,95\%}}$ are between 1 and 20% shorter compared to the 25 kg/h scenario. All basic findings for Table 6 hold here as well. Note that the value $t_{\mathrm{heal,90\%}} = 59.7$ s for $T^{max}_{HS} = 1400$ °C and $T_{hom} = 1000$ °C is exactly the scenario investigated in Figs. 8 and 9 and Table 5.

**Table 6**
Hot spot healing times for 25 kg/h nitrogen flow.

| Surface temp. [°C] | Solar power [kW] | Hot spot temp. [°C] | Hot spot power factor | $t_{\mathrm{heal,90\%}}$ [s] | $t_{\mathrm{heal,95\%}}$ [s] |
|---|---|---|---|---|---|
| 800 | 44.3 | 900 \| 1000 \| 1200 \| 1400 | 2.0 \| 3.2 \| 6.6 \| 11.7 | 95.8 \| 104.4 \| 104.9 \| 106.8 | 172.2 \| 202.9 \| 207.8 \| 215.7 |
| 1000 | 82.5 | 1100 \| 1200 \| 1400 | 1.6 \| 2.4 \| 4.5 | 61.4 \| 61.2 \| 60.9 | 113.5 \| 126.6 \| 133.5 |
| 1200 | 127.5 | 1300 \| 1400 | 1.6 \| 2.4 | 46.0 \| 46.1 | 86.8 \| 95.9 |

**Table 7**
Hot spot healing times for 100 kg/h nitrogen flow.

| Surface temp. [°C] | Solar power [kW] | Hot spot temp. [°C] | Hot spot power factor | $t_{heal,90\%}$ [s] | $t_{heal,95\%}$ [s] |
|---|---|---|---|---|---|
| 800 | 44.3 | 900 \|1000 \| 1200 \| 1400 | 2.0 \| 3.2 \| 6.6 \| 11.7 | 93.7 \| 103.2 \| 104.0 \| 106.2 | 160.0 \| 190.7 \| 205.5 \| 215.1 |
| 1000 | 82.5 | 1100 \| 1200 \| 1400 | 1.6 \| 2.4 \| 5.3 | 54.8 \| 59.6 \| 59.7 | 98.3 \| 118.9 \| 126.8 |
| 1200 | 138.8 | 1300 \| 1400 | 1.6 \| 2.2 | 43.8 \| 39.7 | 82.9 \| 80.8 |

### 4.2. Plant efficiency for nonuniform irradiation

In this section the plant efficiency and generated hydrogen of the cycling process is investigated in case of a general nonuniform irradiation. In praxis this can occur when available heliostats, reactor geometry, and/or positioning on the solar tower do not perfectly match. If only outer heliostats on the left or right of the heliostat field are available, for instance when the field is partly shadowed by clouds or the tower itself, the reactor receives more radiation on its right or left side respectively. In the considered scenarios here, it is assumed that the inclination angle of the reactor is adjusted to the center of the field and kept fixed, while only heliostats closer to the tower are available. Due to this geometric misalignment less irradiation reaches the lower part of the absorber while the upper part is not affected. Here, it has been used the lower third as the area of reduced irradiation for illustration purpose. Three cases are compared: uniform irradiation, full irradiation on the upper two thirds and only half irradiation on the lower third, and only irradiation on the upper two thirds. The cases are denoted as uniform, upper 2/3 + lower 1/3 half, and upper 2/3. The half irradiation on the lower third is meant regarding the solar power density in W/ $m^2$.

The considered operational scenario is a standard temperature swing with 20-min reduction at 1400 °C absorber surface temperature with 100 kg/h nitrogen flow, followed by a 20-min oxidation step at 1000 °C with 15 kg/h steam. Note that reduction and oxidation temperatures are only reached at the fully irradiated areas of the absorber, i.e., for the nonuniform cases only within the upper two thirds. In Table 8 the corresponding results are displayed for the three cases. Note that all values are obtained after steady state cycle conditions have been reached.

In the second column the required total power for keeping the fully irradiated part of the absorber at 1400 °C is given. Note that for the upper 2/3 case much more power is required than just two thirds of the uniform case, i.e., 205 kW vs. 152 kW. This is due to the indirect heating effect of the lower third, mainly due to heat radiation of the upper two thirds, but also due to reflection of solar radiation and conductive heat transfer. The same holds for the required power at the end of the oxidation step in column three. The values for the upper 2/3 + lower 1/3 half case are in between the other cases, which is plausible since the irradiation conditions are in the middle of the uniform and upper 2/3 case. In the fourth column the related average power density at the fully irradiated areas is given for end of reduction and oxidation, respectively.

**Table 8**
Process performance for uniform and nonuniform irradiation.

| Irradiation | Power at end of Red [kW] | Power at end of Ox [kW] | Power density Red \| Ox [kW/ $m^2$] | $H_2$/cycle [g] | $\mu_{plant}$ [%] |
|---|---|---|---|---|---|
| Uniform | 228.4 | 71.6 | 134.4 \| 42.1 | 6.57 | 0.238 |
| Upper 2/3 + lower 1/3 half | 218.0 | 67.3 | 153.9 \| 47.5 | 4.52 | 0.176 |
| Upper 2/3 | 205.2 | 64.3 | 181.1 \| 56.7 | 3.64 | 0.149 |

The power density increases from the uniform to upper 2/3 case, which is due to the increased indirect heat flow towards the not fully irradiated lower third. The absorber surface temperature distribution in the two nonuniformly irradiated cases is given in Fig. 10 a) and c) for the end of reduction. The colder third only has at a temperature difference of around 200 °C to the reduction temperature 1400 °C in the upper 2/3 case and less than 100 °C in the upper 2/3 + lower 1/3 half case. The corresponding temperature plots for the end of oxidation are given in Fig. 11 a) and c), showing a difference of roughly 100 and 50 °C regarding the oxidation temperature of 1000 °C in the upper two thirds.

In the last two columns the resulting generated hydrogen per cycle and related plant efficiency are given. When comparing the uniform and upper 2/3 case, in the latter case less than two thirds of the hydrogen in the uniform case is generated. This is mainly due to the orthogonal conductive heat flows towards the colder third resulting in lower reduction temperatures of all radial layers behind the surface layer in the upper two thirds. Only by partly radiation of the lower third roughly two thirds of the hydrogen of the uniform case can be generated. The corresponding plant efficiency drops to 74% and 63% of the efficiency in the uniform case. Since partly radiation has such a strong negative impact this should be avoided in practical operation whenever possible, as well as it should already be regarded during reactor design and additional potential secondary concentrator geometry layout.

Some words regarding the plant efficiency should be in order. The obtained plant efficiency values in Table 8 are much below the actual practically demonstrated efficiencies of around 5% in smaller scale reactors, cf [18]. The here investigated 250-kW reactor is not designed for temperatures above 1400 °C and has got a comparable large aperture, which are the main reasons for limiting the potential efficiency to roughly 1%, cf. [33,34], whereas practical efficiencies of 0.5% have been demonstrated, cf [39]. The chosen scenarios in this paper are with respect to demonstrating insights gained by a suitable 3D discretization model. The investigated cycle times are longer, and the steam mass flows are smaller compared to the optimal operational strategy in Ref. [33], resulting in a small base case efficiency of 0.24%. However, the purpose of this paper is to reveal the effects of different kinds of nonuniform irradiation, and connected therewith, the influence of the thermal conductivity within such a non-homogeneous case. The general findings of this paper are applicable to other fixed-bed reactors of this type as well, largely independent of their plant efficiencies. The specific impact on temperature, generated hydrogen and efficiency will of course depend on the specific reactor design and operation.

### 4.3. Influence of thermal conductivity

The occurrence of nonuniform absorber irradiation goes along with a significant decrease in efficiency, due to the temperature gap between fully and non-fully irradiated parts, where the latter generate much less hydrogen per surface area. To increase this share, the heat energy of the fully irradiated parts might be used by means of increased orthogonal conduction, and thereby increasing the temperature in the colder parts. This can be done e.g., by replacing the used tape material between the absorber blocks by an adapted version of the tape with larger thermal conductivity. The purpose of the tape is mainly to avoid mechanical abrasion due to micro-movement of the block elements caused by thermal expansion during temperature swing cycling. Besides the increased orthogonal thermal conductivity, the radial thermal conductivity is also partly increased, since the tape also allows for an increased heat flow to the radial back layers, by using the tape as thermal bridge. This effect should also be highly advantageously, since it increases the relatively small temperature difference between reduction and oxidation step at the absorber backside when using the actual design, cf. Fig. 4. Especially when using shorter cycle times, which generally are suited for optimal plant operation, the temperature gap between the process steps at the backside decreases even more, cf [34]. The thermal conductivity of the used tape is 0.5 $W/(m \cdot K)$, which has been increased

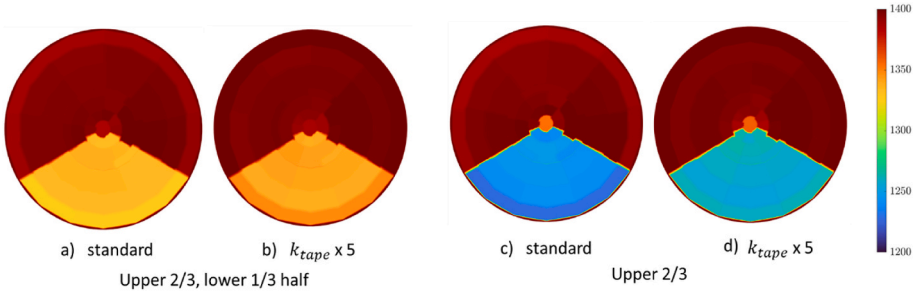


**Fig. 10.** Surface temperature in °C at end of reduction for nonuniform irradiation and varying thermal conductivity of tape.

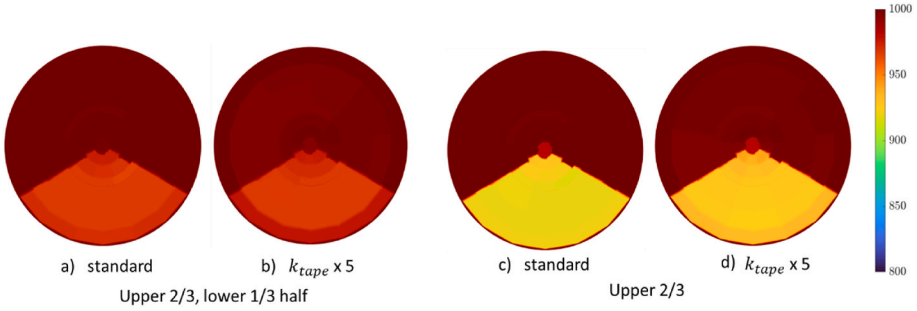


**Fig. 11.** Surface temperature in °C at end of oxidation for nonuniform irradiation and varying thermal conductivity of tape.

in different simulation scenarios by a factor of 2, 5 and 20, thus with a maximal value of 10 $W/(m \cdot K)$. In praxis a tape replacement could be performed during a maintenance activity that requires disassembling the reactor block elements. The corresponding tape materials with increased thermal conductivity are thought to be available on the market.

Further, it has been varied the thermal conductivity of the absorber material. Compared to the replacement of the tape, this adjustment is substantial and non-trivial. The used metal foam consisting of ceria and zirconia has a temperature dependent thermal conductivity and ranges from 0.95 $W/(m \cdot K)$ at 1000 °C to 0.8 $W/(m \cdot K)$ at 1400 °C, which has been increased in the simulation by a factor of 2 and 10. Eventually by inserting several thin radial thermal bridges within the absorber foam blocks these increased values might be realized. This mainly affects the radial thermal conduction, such that back layers have higher reduction temperatures which relate to more generated hydrogen. With larger temperatures of the back layers also the orthogonal heat conduction increases, due to larger temperature differences between fully and non-fully irradiated areas.

In Table 9 generated hydrogen per cycle and plant efficiencies are compared for the three radiation cases and varying thermal conductivity values for tape and absorber material.

The applied operational process conditions for uniform, upper 2/3 + lower 1/3 half, and upper 2/3 case are identical to those described above for Table 8. Thus, the results for the standard thermal conductivity in column two of Table 9 are identical to the last two columns of Table 8. In columns three, four and five the results for an increased thermal conductivity of the tape by a factor of 2, 5 and 20 are presented. In all radiation cases both the amount of generated hydrogen and the plant efficiency increases by roughly 10%, 50% and 100%, respectively. For the upper 2/3 radiation and a five times larger thermal conductivity of tape the amount of hydrogen per cycle is 5.35 g (+47%) and the plant efficiency 0.214% (+44%), whereas for the upper 2/3 + lower 1/3 half case the amount of hydrogen increases to 6.67 g (+48%) and related plant efficiency to 0.255% (+45%). The corresponding surface temperatures for these cases are shown in Figs. 10 and 11 for the end of reduction and oxidation. In the two nonuniformly irradiated cases the positive effect of an increased tape conductivity by a factor of 20 is even larger compared to the uniform case. In the last two columns the results for an increased thermal conductivity of the absorber material are presented. For a factor 2 generated hydrogen and efficiency increase by around 20% in all radiation cases, and for a factor of 10 the nonuniform cases show an increase of 100% for hydrogen and efficiency and a 90% increase in the uniform case. Thus, replacing the tape material by a more thermal conductive one as well as improving the thermal conductivity of the absorber material heavily improves the overall hydrogen generation and thereby the plant efficiency. Note, that the specific size of the beneficial effect heavily depends on the actual absorber design, e.g., with an increased (or reduced) absorber thickness these effects are correspondingly larger or smaller, respectively.

**Table 9**
Process efficiency for different thermal conductivities and nonuniform irradiation.

| Irradiation | $H_2$/cycle [g] \| $\mu_{plant}$ [%] | | | | | |
|---|---|---|---|---|---|---|
| | standard | $k_{tape}$ x2 | $k_{tape}$ x5 | $k_{tape}$ x20 | $k_{Abs}$ x2 | $k_{Abs}$ x10 |
| Uniform | 6.57 \| 0.238 | 7.27 \| 0.263 | 9.37 \| 0.336 | 13.48 \| 0.478 | 7.85 \| 0.284 | 12.56\| 0.449 |
| Upper 2/3 + lower 1/3 half | 4.52 \| 0.176 | 5.01\| 0.193 | 6.67 \| 0.255 | 10.26 \| 0.384 | 5.45 \| 0.211 | 9.23 \| 0.350 |
| Upper 2/3 | 3.64 \| 0.149 | 4.01 \| 0.163 | 5.35 \| 0.214 | 8.62 \| 0.335 | 4.37 \| 0.177 | 7.43 \| 0.296 |

In Fig. 10 a) and b) the surface temperature distribution at the end of reduction is shown for the upper 2/3 + lower 1/3 half case for the standard and 5 times larger tape conductivity.

The upper two thirds are in both cases at 1400 °C since a corresponding controller has been employed in the model. The lower third is colder in the standard case at around 1315 °C, and around 1350 °C in case of increased conductivity. A similar behavior can be observed in Fig. 10 c) and d) for the upper 2/3 case and the same conductivities. Here, the temperature of the lower third increases from 1225 °C to around 1265 °C. Thus, the increased tape conductivity acts as a healing possibility for nonuniform radiation and goes along with an increased efficiency.

In Fig. 11 corresponding surface temperature distributions at the end of oxidation are presented. Hence, the upper two thirds in all cases are at 1000 °C due to the employed heat controller. The temperature of the lower third is only marginally lower in Fig. 11 a) compared to b) with increased conductivity, i.e., with temperatures between 960 and 975 °C. Also, in the upper 2/3 case in Fig. 11 c) and d) the temperature in the colder third only increases from roughly 920–940 °C. In general, at the end of oxidation the temperature gap between fully and non-fully irradiated areas is quite small compared to the end of reduction due to the comparable small difference in solar irradiation.

## 5. Conclusions

In this paper a detailed multi-physical simulation model of a prototype reactor for thermo-chemical water splitting has been presented, with a focus on fine spatial resolution of the absorber. In the first part a radial mesh refinement study is presented demonstrating a suitable level of radial resolution of the model. For spatial discretization of the surface several orthogonal models have been compared, whereby the radial discretization has been set to the 4 + 4 radial mesh as a suitable compromise between performance and accuracy. The finest O9 orthogonal mesh with nearly 28,000 variables has been used for subsequent analyses of different kinds of nonuniform irradiation.

Two types of nonuniform irradiation are analyzed which both practically can occur during operation in the field: the hot spot scenario and general nonuniform irradiation of a larger surface area. First, the conditions and mechanisms for the occurrence and vanishing of hot spots have been analyzed for different absorber and hot spot temperatures. It has been found out, that mainly the absorber temperature determines the hot spot healing process, whereby the hot spot temperature only has a small effect on the healing time. Second, general nonuniform irradiation has been analyzed for the case where the lower third of the absorber is either not or not-fully irradiated. It was found that general nonuniform irradiation significantly decreases hydrogen generation and plant efficiency, in our case study up to −37%. Since this effect is quite significant, even in the case of only locally not-fully irradiation, this must be avoided during operation. Already during design of reactor geometry and potential secondary concentrator it is beneficial to take this aspect into account, especially in view of its usage on a specific solar tower and heliostat field with corresponding target point strategy.

Finally, a small sensitivity study regarding thermal conductivity of tape and absorber material has been conducted in view of nonuniform irradiation. Increasing the thermal conductivity of the tape has a strong positive effect on the efficiency, both, in the uniform and even more in the nonuniform irradiation case. An increase by a factor of 5 yields an increase in efficiency of 50%, and when using a tape with a 20 times larger thermal conductivity the plant efficiency doubles. This significant positive effect of using the tape material as heat bridge should be regarded during reactor design or re-design, especially since the effort for this modification is relatively low. The specific increase of generated hydrogen and plant efficiency depends on the specific layout of the reactor and absorber, e.g., the positive effect for fixed-bed reactors with absorber blocks of shorter radial depths might be smaller. In addition, the heat transfer from front to backside might be improved by optimized material structures using additive manufacturing. More research and measurement campaigns are required for a deeper investigation of the occurring effects and potential remedies for different nonuniform irradiation scenarios.

Nomenclature

| | | |
|---|---|---|
| Symbols | | |
| $A$ | area | $m^2$ |
| $c_p$ | specific heat capacity | $J/(kg \bullet K)$ |
| $E$ | energy | J |
| $E_i$ | irradiance onto element i | $W/m^2$ |
| $F_{i\to j}$ | view factor from element i to j | |
| $H$ | radiosity | $W/m^2$ |
| $k$ | conductivity | $W/(m \cdot K)$ |
| $\dot{m}$ | mass flow rate | kg/s |
| $m$ | mass | kg |
| $n$ | number/empirical parameter | |
| $P$ | power | W |
| $p$ | pressure | bar |
| $\dot{Q}$ | heat flow | W |
| $Q$ | heat | Ws |
| $t$ | time | s |
| $T$ | temperature | K |
| $u$ | fluid velocity | m/s |
| $z$ | radial depth | m |
| Greek Symbols | | |
| $\alpha$ | absorbed | |
| $\delta$ | non-stoichiometric coefficient/reduction extent | |
| $\varepsilon$ | porosity | |
| $\eta$ | efficiency | % |
| $\vartheta$ | temperature | °C |
| $\rho$ | density | $kg/m^3$ |
| $\sigma$ | Stefan Boltzmann constant | $W/(m^2 \cdot K^4)$ |
| $\tau$ | transmitted | |
| Subscripts | | |
| *abs* | absorber | |
| *eff* | effective | |
| *el* | electric | |
| *exgas* | exhaust gas | |
| *f* | fluid phase | |
| *front* | absorber frontside | |
| *heat* | thermal radiation | |
| $i,j,k,\ell,m,p,q$ | element number | |
| *ox* | oxidation | |
| *prod* | production | |
| *R* | reactor | |
| *red* | reduction | |
| *r* | solar/thermal reflection | |
| *s* | solid material | |
| *sol* | solar radiation | |
| *vap* | vaporizer | |
| Abbreviations | | |
| CSR | concentrated solar radiation | |
| *HHV* | higher heating value | J/kg |

## CRediT authorship contribution statement

**Jörg Lampe:** Conceptualization, Methodology, Project administration, Writing – original draft, Writing – review & editing, Software. **Sören Henke:** Data curation, Investigation, Software, Validation, Visualization, Writing – review & editing. **Steffen Menz:** Validation, Writing – review & editing, Software. **Thomas Fend:** Project administration, Resources, Visualization.

## Declaration of competing interest

The authors declare that they have no known competing financial interests or personal relationships that could have appeared to influence the work reported in this paper.

## Acknowledgements

Funding has been received for this work within the framework of project ASTOR_ST, under the grant number KESW-1-2-011A, supported by the European Regional Development Fund and the North Rhine-Westphalia Ministry of Economic Affairs, Innovation, Digitalization & Energy.

## Appendix

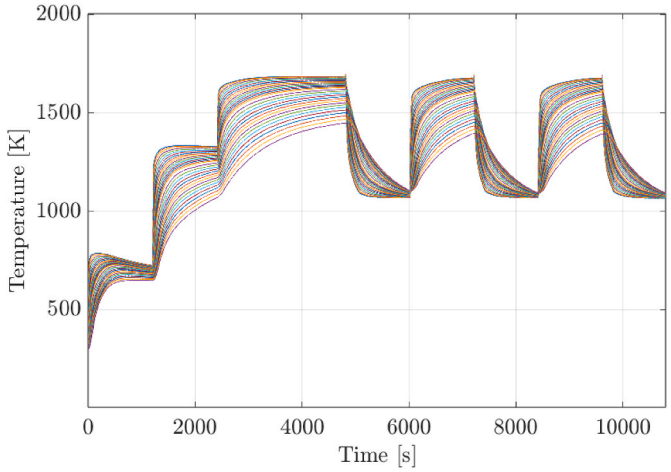


**Fig. 12.** Temperature behavior of all radial layers of 16 + 16 mesh during process operation.

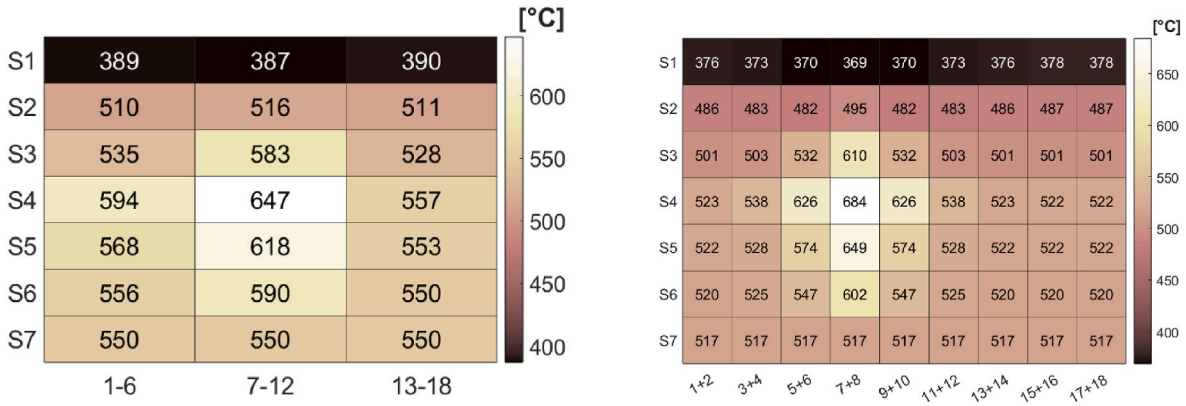


**Fig. 13.** Temperature of absorber backside at end of reduction – O3 mesh (left), O9 mesh (right).

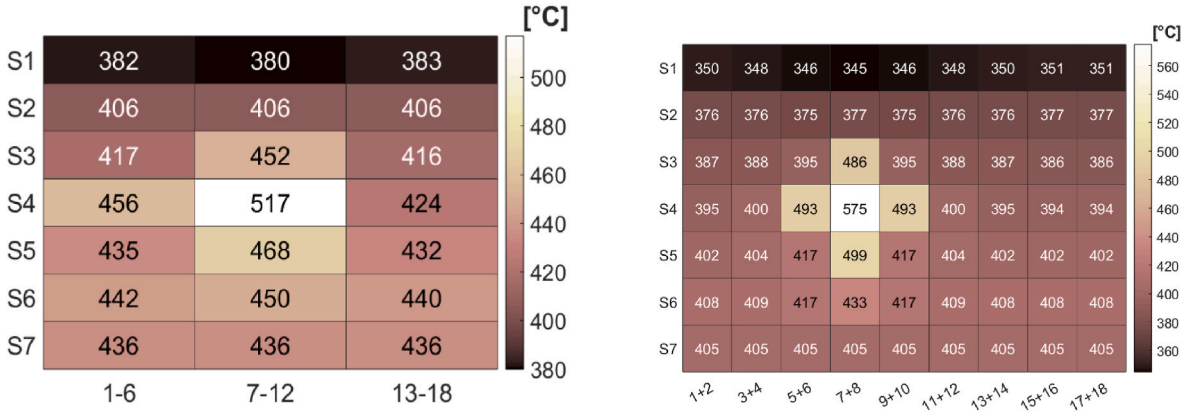


**Fig 14.** Temperature of absorber surface at end of oxidation – O3 mesh (left), O9 mesh (right).

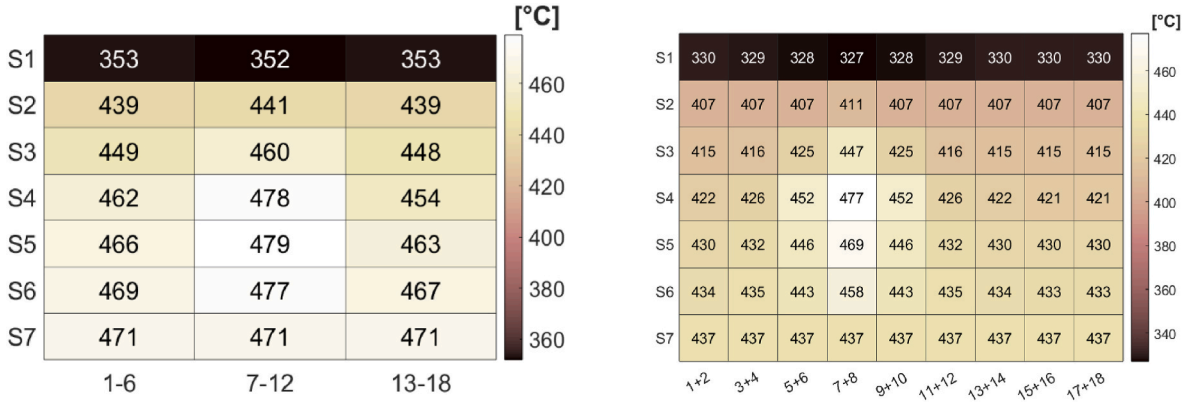


**Fig. 15.** Temperature of absorber backside at end of oxidation – O3 mesh (left), O9 mesh (right).

## References


[1] Fan L, Tu Z, Chan SH. Recent development of hydrogen and fuel cell technologies: a review. Energy Rep 2021;7:8421e46. https://doi.org/10.1016/j.egyr.2021.08.003.

[2] Nieves Camacho Md l, Jurburg D, Tanco M. Hydrogen fuel cell heavy-duty trucks: review of main research topics. Int J Hydrogen Energy 2022;47:29505e25. https://doi.org/10.1016/j.ijhydene.2022.06.271.

[3] Sudharshan Ravi S, Aziz M. Clean hydrogen for mobility e quo vadis? Int J Hydrogen Energy 2022;47:20632e61. https://doi.org/10.1016/j.ijhydene.2022.04.158.

[4] Liu W, Zuo H, Wang J, Xue Q, Ren B, Yang F. The production and application of hydrogen in steel industry. Int J Hydrogen Energy 2021;46:10548e69. https://doi.org/10.1016/j.ijhydene.2020.12.123.

[5] Kullmann F, Linßen J, Stolten D. The role of hydrogen for the defossilization of the German chemical industry. Int J Hydrogen Energy 2023;48(99):38936–52. https://doi.org/10.1016/j.ijhydene.2023.04.191.

[6] Abdellatif M, Hashemi M, Azizmohammadi S. Large-scale underground hydrogen storage: integrated modeling of reservoir-wellbore system. Int J Hydrogen Energy 2023;48(50):19160e71. https://doi.org/10.1016/j.ijhydene.2023.01.227.

[7] Mehr AS, Phillips AD, Brandon MP, Pryce MT, Carton JG. Recent challenges and development of technical and technoeconomic aspects for hydrogen storage, insights at different scales; A state of art review. Int J Hydrogen Energy 2024;70:786–815. https://doi.org/10.1016/j.ijhydene.2024.05.182.

[8] Zeng D, Li M, Qiu Y, Ma L, Cui D, Zhang S, Xiao R. A high-performance ternary ferrite-spinel material for hydrogen storage via chemical looping redox cycles. Int J Hydrogen Energy 2020;45:2034–43. https://doi.org/10.1016/j.ijhydene.2019.11.021.

[9] Le Gallo Y. Assessment of hydrogen storage capacity in porous media at the European scale. Int J Hydrogen Energy 2024;58:400–8. https://doi.org/10.1016/j.ijhydene.2024.01.158.

[10] Kadar J, Gackstatter F, Ortner F, Wagner L, Willer M, Preuster P, Wasserscheid P, Geißelbrecht M. Boosting power density of hydrogen release from LOHC systems by an inverted fixed-bed reactor design. Int J Hydrogen Energy 2024;59:1376–87. https://doi.org/10.1016/j.ijhydene.2024.02.096.

[11] Kovač A, Paranos M, Marciuš D. Hydrogen in energy transition: a review. Int J Hydrogen Energy 2021;46(6):10016–35. https://doi.org/10.1016/j.ijhydene.2020.11.256.

[12] Tariq AH, Anwar M, Abbas Kazmi SA, Hassan M, Bahadar A. Techno-economic and composite performance assessment of fuel cell-based hybrid energy systems for green hydrogen production and heat recovery. Int J Hydrogen Energy 2024. https://doi.org/10.1016/j.ijhydene.2024.04.018. in press.

[13] Sadeghian O, Shotorbani AM, Ghassemzadeh S, Mohammadi-Ivatloo B. Energy management of hybrid fuel cell and renewable energy based systems - a review. Int J Hydrogen Energy 2024. https://doi.org/10.1016/j.ijhydene.2024.03.134. in press.

[14] Van LP, Chi KD, Duc TN. Review of hydrogen technologies based microgrid: energy management systems, challenges and future recommendations. Int J Hydrogen Energy 2023;48:14127–48. https://doi.org/10.1016/j.ijhydene.2022.12.345.

[15] Goikoetxea NB, Gómez-Mancebo MB, Fernández-Saavedra R, Borlaf F, García-Pérez F, Jiménez JA, Llorente I, Rucandio I, Quejido AJ. Understanding water-splitting thermochemical cycles based on nickel and cobalt ferrites for hydrogen production. Int J Hydrogen Energy 2019;44(33):17578–85. https://doi.org/10.1016/j.ijhydene.2019.05.003.

[16] Mao Y, Gao Y, Dong W, Wu H, Song Z, Zhao X, Sun J, Wang W. Hydrogen production via a two-step water splitting thermochemical cycle based on metal oxide – a review. Appl Energy 2020;267:114860. https://doi.org/10.1016/j.apenergy.2020.114860.

[17] Chuayboon S, Abanades S. An overview of solar decarbonization processes, reacting oxide materials, and thermochemical reactors for hydrogen and syngas production. Int J Hydrogen Energy 2020;45:25783–810. https://doi.org/10.1016/j.ijhydene.2020.04.098.

[18] Marxer D, Furler P, Takacs M, Steinfeld A. Solar thermochemical splitting of CO2 into separate streams of CO and O2 with high selectivity, stability, conversion, and efficiency. Energy Environ Sci 2017;10(5):1142–9. https://doi.org/10.1039/C6EE03776C.

[19] Houaijia A, Sattler C, Roeb M, Lange M, Breuer S, Säck JP. Analysis and improvement of a high-efficiency solar cavity reactor design for a two-step thermochemical cycle for solar hydrogen production from water. Sol Energy 2013;97:26–38. https://doi.org/10.1016/j.solener.2013.07.032.

[20] Venstrom LJ, de Smith RM, Hao Y, Haile SM, Davidson JH. Efficient splitting of CO2 in an isothermal redox cycle based on ceria. Energy Fuels 2014;28(4):2732–42. https://doi.org/10.1021/ef402492e.

[21] Ermanoski I, Siegel NP, Stechel EB. A new reactor concept for efficient solar-thermochemical fuel production. J Sol Energy Eng 2013;135(3). https://doi.org/10.1115/1.4023356.

[22] Kodama T, Goko M, Cho HS, Bellam S, Matsubara K, Inoue K. Particles fluidized bed receiver/reactor with a beam-down solar concentrating optics: 30-kWth performance test using a big sun-simulator. AIP Conf Proc 2017;1734(1):120004. https://doi.org/10.1063/1.494920.

[23] Chueh WC, Haile SM. A thermochemical study of ceria: exploiting an old material for new modes of energy conversion and CO2 mitigation. Philos Trans A Math Phys Eng Sci 2010;368(1923):3269–94. https://doi.org/10.1098/rsta.2010.0114.

[24] Lin M, Haussener S. Solar fuel processing efficiency for ceria redox cycling using alternative oxygen partial pressure reduction methods. Energy 2015;88:667–79. https://doi.org/10.1016/j.energy.2015.06.006.

[25] Lu Y, Zhu L, Agrafiotis C, Vieten J, Roeb M, Sattler C. Solar fuels production: two-step thermochemical cycles with cerium-based oxides. Prog Energy Combust Sci 2019;75:100785. https://doi.org/10.1016/j.pecs.2019.100785.

[26] Bhosale RR, Takalkar G, Sutar P, Kumar A, AlMomani F, Khraisheh M. A decade of ceria based solar thermochemical H2O/CO2 splitting cycle. Int J Hydrogen Energy 2019;44(1):34–60. https://doi.org/10.1016/j.ijhydene.2018.04.080.

[27] Hoes M, Ackermann S, Theiler D, Furler P, Steinfeld A. Additive-manufactured ordered porous structures made of ceria for concentrating solar applications. Energy Technol 2019;7(9):1900484. https://doi.org/10.1002/ente.201900484.

[28] Gager E, Frye M, McCord D, Scheffe J, Nino JC. Reticulated porous lanthanum strontium manganite structures for solar thermochemical hydrogen production. Int J Hydrogen Energy 2022;47(73):31152–64. https://doi.org/10.1016/j.ijhydene.2022.07.052.

[29] Ji HI, Davenport TC, Gopal CB, Haile SM. Extreme high temperature redox kinetics in ceria: exploration of the transition from gas-phase to material-kinetic limitations. Phys Chem Chem Phys: Phys Chem Chem Phys 2016;18(31):21554–61. https://doi.org/10.1039/c6cp01935h.

[30] Bulfin B, Call F, Vieten J, Roeb M, Sattler C, Shvets IV. Oxidation and reduction reaction kinetics of mixed cerium zirconium oxides. J Phys Chem C 2016;120(4):2027–35. https://doi.org/10.1021/acs.jpcc.5b08729.

[31] Muhich CL, Blaser S, Hoes MC, Steinfeld A. Comparing the solar-to-fuel energy conversion efficiency of ceria and perovskite based thermochemical redox cycles for splitting H2O and CO2. Int J Hydrogen Energy 2018;43(41):18814–31. https://doi.org/10.1016/j.ijhydene.2018.08.137.

[32] Bayon A, de La Calle A, Ghose KK, Page A, McNaughton R. Experimental, computational and thermodynamic studies in perovskites metal oxides for thermochemical fuel production: a review. Int J Hydrogen Energy 2020;45(23):12653–79. https://doi.org/10.1016/j.ijhydene.2020.02.126.

[33] Lampe J, Menz S, Akinci K, Böhm K, Seeger T, Fend T. Optimizing the operational strategy of a solar-driven reactor for thermochemical hydrogen production. Int J Hydrogen Energy 2022;47:14453–68. https://doi.org/10.1016/j.ijhydene.2022.02.193.

[34] Lampe J, Menz S. Optimized operational strategy of a solar reactor for thermochemical hydrogen generation. Optim Eng 2023. https://doi.org/10.1007/s11081-023-09855-3.
[35] Brendelberger S, Rosenstiel A, Lopez-Roman A, Prieto C, Sattler C. Performance analysis of operational strategies for monolithic receiver-reactor arrays in solar thermochemical hydrogen production plants. Int J Hydrogen Energy 2020;45(49):26104–16. https://doi.org/10.1016/j.ijhydene.2020.06.191.
[36] Moser M, Pecchi M, Fend T. Techno-economic assessment of solar hydrogen production by means of thermo-chemical cycles. Energies 2019;12(3):352. https://doi.org/10.3390/en12030352.
[37] Budama VK, Johnson NG, Ermanoski I, Stechel EB. Techno-economic analysis of thermochemical water-splitting system for Co-production of hydrogen and electricity. Int J Hydrogen Energy 2021;46(2):1656–70. https://doi.org/10.1016/j.ijhydene.2020.10.060.
[38] Boretti A, Castelletto S, De Angelis F. A solar concentrator/receiver/storage/reactor system for thermochemical splitting cycles based on perovskites. Int J Hydrogen Energy 2022;47(7):4970–5. https://doi.org/10.1016/j.ijhydene.2021.11.094.
[39] Thanda VK, Fend T, Laaber D, Lidor A, von Storch H, Säck JP, Hertel J, Lampe J, Menz S, Piesche G, Berger S, Lorentzou S, Syrigou M, Denk T, Gonzales-Pardo A, Vidal A, Roeb M, Sattler C. Experimental investigation of the applicability of a 250 kW ceria receiver/reactor for solar thermochemical hydrogen generation. Renew Energy 2022;198:389–98.
[40] Menz S, Lampe J, Tröltzsch U, Weiler P, Pahl A, Fend T, Seeger T. Real time executable model for dynamic heat flow analysis of a solar hydrogen reactor. TM - Tech Mess 2020;(87):360–71. https://doi.org/10.1515/teme-2019-0128.
[41] Menz S, Lampe J, Krause J, Seeger T, Fend T. Holistic energy flow analysis of a solar driven thermo-chemical reactor set-up for sustainable hydrogen production. Renew Energy 2022;189:1358–74. https://doi.org/10.1016/j.renene.2022.03.033.
[42] Menz S, Lampe J, Henke S, Seeger T. Physical system behavior and energy flow analysis of a solar driven hydrogen production plant based on two-step thermochemical redox cycles. Int J Hydrogen Energy 2023. https://doi.org/10.1016/j.ijhydene.2023.06.112.
[43] Houaijia A, Sattler C, Roeb M, Lange M, Breuer S, Säck JP. Analysis and improvement of a high-efficiency solar cavity reactor design for a two-step thermochemical cycle for solar hydrogen production from water. Sol Energy 2013;97:26–38. https://doi.org/10.1016/j.solener.2013.07.032.
[44] Lorentzou S, Zygogianni A, Pagkoura C, Karagiannakis G, Konstandopoulos AG, Saeck JP, Breuer S, Lange M, Lapp J, Fend T, Roeb M, Gonzalez A, Vidal Delgado A, Brouwer JP, Makkus RC, Kiartzis SJ. HYDROSOL-PLANT: structured redox reactors for H2 production from solar thermochemical H2O splitting. AIP Conf Proc 2018;130010. 2033.
[45] Bulfin B, Lange M, de Oliveira L, Roeb M, Sattler C. Solar thermochemical hydrogen production using ceria zirconia solid solutions: efficiency analysis. Int J Hydrogen Energy 2016;41(42):19320–8. https://doi.org/10.1016/j.ijhydene.2016.05.211.
[46] Bulfin B, Lowe AJ, Keogh KA, Murphy BE, Lübben O, Krasnikov SA, Shvets IV. Analytical model of CeO2 oxidation and reduction. ACS Journal of Physical Chemistry 2013;117(46):24129–37. https://doi.org/10.1021/jp406578z.
[47] Lapp J, Davidson JH, Lipiński W. Efficiency of two-step solar thermochemical non-stoichiometric redox cycles with heat recovery. Energy 2012;37(1):591–600. https://doi.org/10.1016/j.energy.2011.10.045.
[48] Krenzke PT, Davidson JH. On the efficiency of solar H2 and CO production via the thermochemical cerium oxide redox cycle: the option of inert-swept reduction. Energy Fuel 2015;29(2):1045–54. https://doi.org/10.1021/ef502601f.
[49] Hathaway BJ, Bala Chandran R, Sedler S, Thomas D, Gladen A, Chase T, Davidson JH. Effect of flow rates on operation of a solar thermochemical reactor for splitting CO 2 via the isothermal ceria redox cycle. J Sol Energy Eng 2015;138(1):011007. https://doi.org/10.1115/1.4032019.
[50] Ji HI, Davenport TC, Gopal CB, Haile SM. Extreme high temperature redox kinetics in ceria: exploration of the transition from gas-phase to material-kinetic limitations. Phys Chem Chem Phys: Phys Chem Chem Phys 2016;18(31):21554–61. https://doi.org/10.1039/c6cp01935h.
[51] Zhu L, Lu Y. Reactivity and efficiency of ceria-based oxides for solar CO2 splitting via isothermal and near-isothermal cycles. Energy Fuels 2018;32(1):736–46. https://doi.org/10.1021/acs.energyfuels.7b03284.
[52] Hao Y, Yang CK, Haile SM. High-temperature isothermal chemical cycling for solar-driven fuel production. Phys Chem Chem Phys: Phys Chem Chem Phys 2013;15(40):17084–92. https://doi.org/10.1039/c3cp53270d.
[53] Al-Shankiti I, Ehrhart BD, Weimer AW. Isothermal redox for H2O and CO2 splitting – a review and perspective. Sol Energy 2017;156:21–9. https://doi.org/10.1016/j.solener.2017.05.028.
[54] Hathaway BJ, Bala Chandran R, Gladen AC, Chase TR, Davidson JH. Demonstration of a solar reactor for carbon dioxide splitting via the isothermal ceria redox cycle and practical implications. Energy Fuel 2016;30(8):6654–61. https://doi.org/10.1021/acs.energyfuels.6b01265.
[55] Bulfin B, Call F, Lange M, Lübben O, Sattler C, Pitz-Paal R, Shvets IV. Thermodynamics of CeO2 thermochemical fuel production. Energy Fuels 2015;29(2):1001e9. https://doi.org/10.1021/ef5019912.
[56] MathWorks. Matlab Simscape. https://www.mathworks.com/products/simscape.html. [Accessed 15 December 2022].
[57] Keene DJ, Davidson JH, Lipiński W. A model of transient heat and mass transfer in a heterogeneous medium of ceria undergoing nonstoichiometric reduction. J Heat Tran 2013;135(5). https://doi.org/10.1115/1.4023494.
[58] Suter S, Steinfeld A, Haussener S. Pore-level engineering of macroporous media for increased performance of solar-driven thermochemical fuel processing. Int J Heat Mass Tran 2014;78:688–98. https://doi.org/10.1016/j.ijheatmasstransfer.2014.07.020.
[59] Heraeus, Manufacturers technical documentation: Quartz Glass for Optics, Optical Properties, http://www.heraeus.com, accessed 6 December 2019.
[60] Säck JP, Breuer S, Cotelli P, Houaijia A, Lange M, Wullenkord M, Spenke C, Roeb M, Sattler C. High temperature hydrogen production: design of a 750 KW demonstration plant for a two step thermochemical cycle. Sol Energy 2016;135:232–41.
[61] Palumbo R, Keunecke M, Möller S, Steinfeld A. Reflections on the design of solar thermal chemical reactors: thoughts in transformation. Energy 2004;29:727–44.
[62] Ansys, Inc. R2. ANSYS; 2021. https://www.ansys.com.
[63] Säck JP, Breuer S, Cotelli P, Houaijia A, Lange M, Wullenkord M, Spenke C, Roeb M, Sattler C. One year with synlight – review of operating experience. AIP Conf Proc 2019;2126:170007. https://doi.org/10.1063/1.5117677.